RIVM report 481508017/2004

The Atmosphere-Ocean System of IMAGE 2.2
A global model approach for atmospheric concentrations, and climate and sea level projections

B. Eickhout, M.G.J. den Elzen and
G.J.J. Kreileman*

* Currently working at ASML the Netherlands (Veldhoven).

This research was conducted for the Dutch Ministry of Housing, Spatial Planning and the Environment as part of the Project for IMAGE Adaptation and Maintenance (M/481508 IMAGE Aanpassing en Beheer).

RIVM, P.O. Box 1, 3720 BA Bilthoven, telephone: 31 - 30 - 274 91 11; telefax: 31 - 30 - 274 29 71

National Institute for Public Health and the Environment (RIVM)
Global Sustainability and Climate (KMD)
Netherlands Environmental Assessment Agency
P.O. Box 1, 3720 BA Bilthoven
The Netherlands
Telephone : +31 30 2742924
Fax : +31 30 2744464
E-mail : Bas.Eickhout@rivm.nl
Website : http://www.rivm.nl/ieweb

Abstract

Here, we describe the technical background of the Atmosphere Ocean System (AOS) of the Integrated Model to Assess the Global Environment (IMAGE, version 2.2). The AOS submodel elaborates the global concentrations of the most important greenhouse gases and ozone precursors, along with their direct and indirect effects on global-mean radiative forcing. These submodels are based on state-of-the-art approximations, as published by the Intergovernmental Panel on Climate Change (IPCC) in its Third Assessment Report (TAR). That these simple submodels can adequately reproduce the global concentrations and forcings of more complex models in a very short runtime is also true for the simple climate submodel for calculating the consequences for the climate system and sea-level rise described in this report. We also elaborate on the scientific background and the most important features of the different submodels, comparing the results with other models and observations. Furthermore, we demonstrate that AOS adequately represents the 1970-1995 period for the main global indicators (concentrations, temperature increase and sea-level rise).

Acknowledgements

This report is based on the research conducted by the Dutch National Institute for Public Health and the Environment (RIVM) for the Dutch Ministry of Housing, Spatial Planning and the Environment as part of the IMAGE Adaptation and Maintenance Project.
The authors would like to thank Tom Wigley and Mike Hulme for the distribution of the MAGICC model and Sarah Raper for her very kind support in implementing MAGICC in IMAGE. Furthermore, we would like to thank Fortunat Joos from the University of Bern for his assistance in the implementation of the oceanic carbon model in IMAGE. Michael Schlesinger and Sergej Malyshev kindly provided the data and assistance for implementation of the geographical pattern-scaling with special attention paid to sulphur emissions. We are also grateful to our RIVM colleagues, in particular Bart Strengers, Michiel Schaeffer, Lex Bouwman, Tom Kram and Bert Metz, for their comments and contributions, and Ruth de Wijs for language-editing assistance.

Contents

Samenvatting

Dit rapport beschrijft de technische achtergrond van het atmosfeer-oceaan systeem van het IMAGE-model (Integrated Model to Assess the Global Environment). Het atmosfeer-oceaan systeem van IMAGE modelleert de atmosferische concentraties van de meest belangrijke broeikasgassen en de directe en indirecte effecten van die gassen op de stralingsbalans. Deze submodellen zijn gebaseerd op state-of-the-art benaderingen van meer complexe modellen, zoals gepubliceerd in de Third Assessment Report van het IPCC (Intergovernmental Panel on Climate Change). Dit geldt ook voor het eenvoudige klimaatmodel, wat in dit rapport wordt beschreven en wat de mondiaal gemiddelde klimaatverandering en zeespiegelstijging berekent. Naast de belangrijkste kenmerken van de submodellen, wordt ook de meest relevante wetenschappelijke achtergrond geschetst. Eveneens worden voor een aantal mondiale indicatoren de resultaten vergeleken met observaties en resultaten van meer complexe modellen en wordt aangetoond voor deze indicatoren dat het atmosfeer-oceaan systeem in de periode 1970 – 1995 goed benadert. Elk hoofdstuk wordt afgesloten met projecties tot 2100 volgens de SRES scenario's van het IPCC, zoals die door het IMAGE team in 2001 zijn gepubliceerd.

1. Introduction

The Atmosphere-Ocean System (AOS) is part of the modelling framework, Integrated Model to Assess the Global Environment (IMAGE). IMAGE belongs to the category called 'integrated assessment models', models used for describing the environmental consequences of human activities. More specifically, the objective of the IMAGE model is to explore the long-term dynamics of global environmental change, taking many feedback mechanisms within the society-biosphere-climate system into account.

The IMAGE 2.2 model[1] is an integration of many disciplinary models (see Figure 1.1). Throughout the model, interactions and feedbacks are modelled explicitly. In the IMAGE framework, the general equilibrium economy model, WorldScan (CPB, 1999), and the population model, PHOENIX (Hilderink, 1999), supply the basic information on economic and demographic developments for 17 socio-economic regions (these regions are depicted in Figure 1.2) into the following linked components:

- The Energy-Industry System (EIS) consists of the TIMER and TIMER emissions model (TEM). TIMER calculates regional energy consumption, energy efficiency improvements, fuel substitution, supply and trade of fossil fuels and renewable energy technologies. On the basis of energy use and industrial production, TEM computes emissions of greenhouse gases (GHGs), ozone precursors (CO, NO_x and NMVOC) and sulphur dioxide (SO_2). For further details on TIMER and TEM we refer the reader to De Vries et al. (2001) and IMAGE team (2001a).
- The Terrestrial-Environmental System (TES) consists of an ecosystem model (the Terrestrial Vegetation Model, TVM), a crop model (part of TVM), an agricultural demand model (the Agricultural Demand Model; ADM) and a land-use model (the Land Cover Model; LCM). In TES the land use is dynamically computed on a grid of 0.5 by 0.5 degrees on the basis of regional consumption, production and trading of food, animal feed, fodder, grass and timber, and local climatic and terrain properties. In the Land-Use Emissions Model (LUEM) emissions from land-use change, natural ecosystems and agricultural production systems are computed. The exchange of CO_2 between terrestrial ecosystems and the atmosphere are computed in the Terrestrial Carbon Model (TCM) on the same grid scale. For further details on TES we refer the reader to Alcamo et al. (1998) and IMAGE team (2001a). ADM is documented in Strengers (2001). Results from LUEM and TCM are described in Strengers et al. (2002) and Leemans et al. (2002), respectively.
- The Atmosphere-Ocean System (AOS) calculates changes in atmospheric composition by employing the emissions and by taking oceanic CO_2 uptake and atmospheric chemistry into consideration. Subsequently, changes in climatic properties are computed by resolving the changes in radiative forcing caused by GHGs, aerosols and oceanic heat transport. AOS calculates the globally averaged concentrations, radiative forcings and temperatures.
- The impact models encompass specific models for sea-level rise and land degradation, and make use of specific features of the ecosystem and crop models to depict impacts on vegetation. The ecosystem models include an algorithm that estimates the carbon-cycle consequences of different assumptions for the speed of climate-change induced vegetation migration (Van Minnen et al., 2000).

[1] The IMAGE 2.2 model version, an update of the IMAGE 2.1 model (Alcamo et al., 1998), was released in July 2001 (IMAGE team, 2001a).

The IMAGE 2.2 model differs from the earlier version, IMAGE 2.1(Alcamo et al., 1998) with respect to the following:

- The base year was updated to 1995 (from 1990 in IMAGE 2.1)[2].
- The number of world regions was extended from 13 to 19[3] (including Antarctica and Greenland as separate regions) to reduce some of the obvious problems in heterogeneous regions like Africa and South America, and to enhance the applicability of land-use applications.
- The simple IMAGE 2.1 energy-demand model was replaced with the more comprehensive TIMER energy-demand-and-supply model (De Vries et al., 2001).
- The food demand model in IMAGE 2.1 was replaced by a model based on aggregated food products so as to improve the simulation of income-induced dietary changes (Strengers, 2001).
- The Atmosphere-Ocean System (AOS) was updated by a set of state-of-the-art global-mean models.

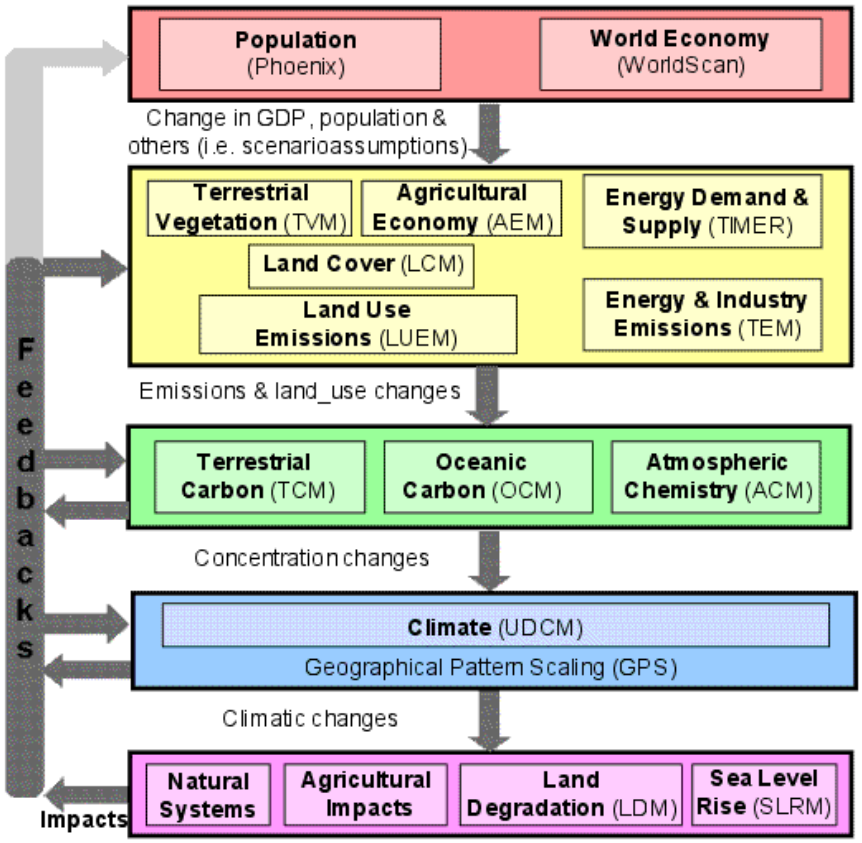

Figure 1.1 Schematic overview of IMAGE 2.2 (IMAGE team, 2001a). The Atmosphere-Ocean System consists of the Oceanic Carbon model, the Atmospheric Chemistry model, the (Upwelling-Diffusion) Climate model and the Sea-Level Rise model[4].

[2] The IMAGE 2.2 model is calibrated on historical data, from 1970 to 1995. The model starts its scenario simulation after this period. The 2.1 version started the scenario simulation in 1990.

[3] Basically we split the African region into four subregions (Northern, Western, Eastern and Southern Africa) and the Latin America region into Central and South America.

[4] The Terrestrial Carbon Model (TCM) of IMAGE 2.2 forms part of the Terrestrial Environment System (TES). This distinction is made because of the grid detail of TCM (0.5 by 0.5 degrees) compared to the global-mean scale of OCM.

This report focuses on AOS in IMAGE 2.2, and its improvements, compared to AOS in IMAGE 2.0 (De Haan et al., 1994; Krol and van der Woerd, 1994) and 2.1 (Alcamo et al., 1998). The results of AOS are also given for the IMAGE 2.2 implementation of the SRES scenarios (Special Report on Emission Scenarios; hereafter known as 'IMAGE 2.2 SRES scenarios'), introduced by the Intergovernmental Panel on Climate Change (IPCC, 2000). The complete implementation of the SRES scenarios and its consequences for concentrations, impacts and climate can be found on the IMAGE 2.2 CD-ROMs (IMAGE team, 2001a; IMAGE team, 2001b).[5]

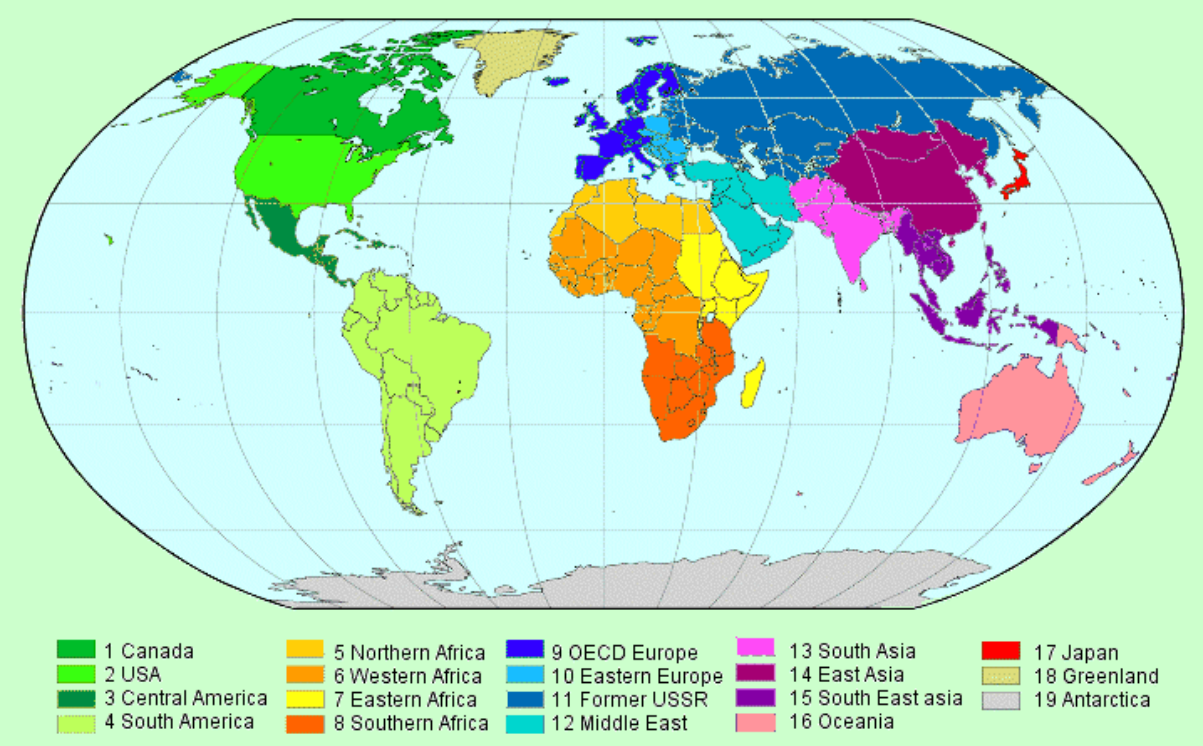

Figure 1.2 The 17 IMAGE 2.2 world regions plus Greenland and Antarctica (IMAGE team, 2001a).

AOS, including the different models of AOS and their interrelationships, is introduced in Chapter 2, along with the differences to AOS in IMAGE 2.0 and 2.1. The forthcoming chapters go on to explain in detail the different AOS components. For example, Chapter 3, explains how the different atmospheric concentrations are calculated, and Chapter 4 describes the modelling of the radiative forcings. The temperature change calculation and its consequences for sea-level rise are described in Chapter 5, while Chapter 6 elaborates on the downscaling of the global-mean temperature change to 0.5 x 0.5 degrees using the General Circulation Model (GCM). Each chapter is concluded with projections for the SRES (Special Report on Emission Scenarios) scenarios of the Intergovernmental Panel on Climate Change, as published by the IMAGE team in 2001.

[5] These CD-ROMs can be ordered from http://www.rivm.nl/ieweb. For further information on the SRES scenarios the reader is referred to IPCC (2000).

2. The Atmosphere-Ocean System: A bird's eye-view

The main goal of AOS is to compute transient changes in climate resulting from changes in greenhouse gas emissions, and to do it in a way that is computationally more economic than a 3-dimensional atmospheric chemistry model coupled with an Atmosphere-Ocean General Circulation Model (AO-GCM). This makes it feasible to dynamically link AOS with the Terrestrial-Environmental System (TES), and makes it possible to use the entire IMAGE 2.2 model iteratively for policy analysis. These faster computations are obtained at the expense of a lower degree of specification as compared to GCMs and 3-dimensional atmospheric chemistry models. This approach also makes it possible to investigate different feedbacks and linkages between the society-biosphere-climate system, which cannot be done with a complex 3-dimensional coupling of atmosphere and ocean models. Here, the submodels of AOS are briefly introduced, along with the reasons why we replace some of the old IMAGE 2.1 submodels by others.

2.1 The models of the Atmosphere-Ocean System of IMAGE

AOS consists of four core models, i.e. the Oceanic Carbon Model, the Atmospheric Chemistry Model, the Upwelling-Diffusion Climate Model and the Sea-Level Rise Model. These models are zero-dimensional or one-dimensional global-mean models. The most important variables (global temperature and precipitation change) are scaled to the TES grid level (0.5 by 0.5 degrees) by the Geographical Pattern Scaling model (GPS) to allow linkage with the IMAGE 2.2 Terrestrial-Environmental System (TES). Figure 2.1 shows the linkages between the AOS models in terms of input and output variables.

AOS consists of the following five models (see Figure 2.1):

- The Atmospheric Chemistry Model (ACM). ACM, an updated version of the IMAGE 2.1 globally averaged chemistry module (Krol and Van der Woerd, 1994), calculates the atmospheric build-up of greenhouse gases and other atmospheric substances relevant to global change. The emissions of methane (CH_4), nitrogenous oxide (N_2O), carbon monoxide (CO), non-methane volatile organic compounds (NMVOC), nitrogen oxides (NO_x) and halocarbons (CFCs, HCFCs, HFCs, Halon-1211, Halon-1301 and CH_3Br) are used as input. The atmospheric concentrations of CH_4, N_2O, CO, the OH radical and tropospheric ozone (O_3) are calculated by the ACM.
- The Oceanic Carbon Model (OCM). OCM, which calculates the carbon uptake by the oceans, consists of a global-mean response function that responds to changes in anthropogenic and terrestrial CO_2 fluxes and changes in the temperature of the oceanic mixed layer. The output of OCM is the net flux of CO_2 and, consequently, its atmospheric concentration. OCM is based on the Bern Oceanic Carbon Cycle model (Joos et al., 1996)[6].
- The Upwelling-Diffusion Climate Model (UDCM). First, UDCM converts the concentrations of the greenhouse gases (from OCM and ACM) and SO_2 emissions (from TES and EIS) into radiative forcings. These calculations are updated in line with the Third Assessment Report (TAR) of the Intergovernmental Panel on Climate Change (IPCC, hereafter shortly referred to as IPCC-TAR; IPCC, 2001). Secondly, the radiative forcings are used as input to calculate the global-mean surface and ocean temperature change. The latter part is based on the MAGICC climate model (Hulme et al., 2000)[7].

[6] OCM was kindly provided by Fortunat Joos.
[7] MAGICC was kindly provided by Tom Wigley, Mike Hulme and Sarah Raper

- The Geographical Pattern Scaling Model (GPS). GPS scales the global-mean surface temperature change to a grid level of 0.5 by 0.5 degrees. This scaling is applied to temperature change and precipitation change. GCM results based on experiments with forcing from sulphate only are also used to take the non-linear regional effects of sulphate aerosols into account. Results from the AGC/MLO model (11-layer troposphere/lower-stratosphere general circulation/mixed-layer-ocean) from the University of Illinois at Urbana-Champaign (UIUC) are used for these sulphate-only patterns [8]. The complete method is described by Schlesinger et al. (2000).
- The Sea-Level Rise Model (SLRM). SLRM is based on the sea-level rise model of the MAGICC climate model (Raper et al., 1996) and calculates the global mean sea-level rise.

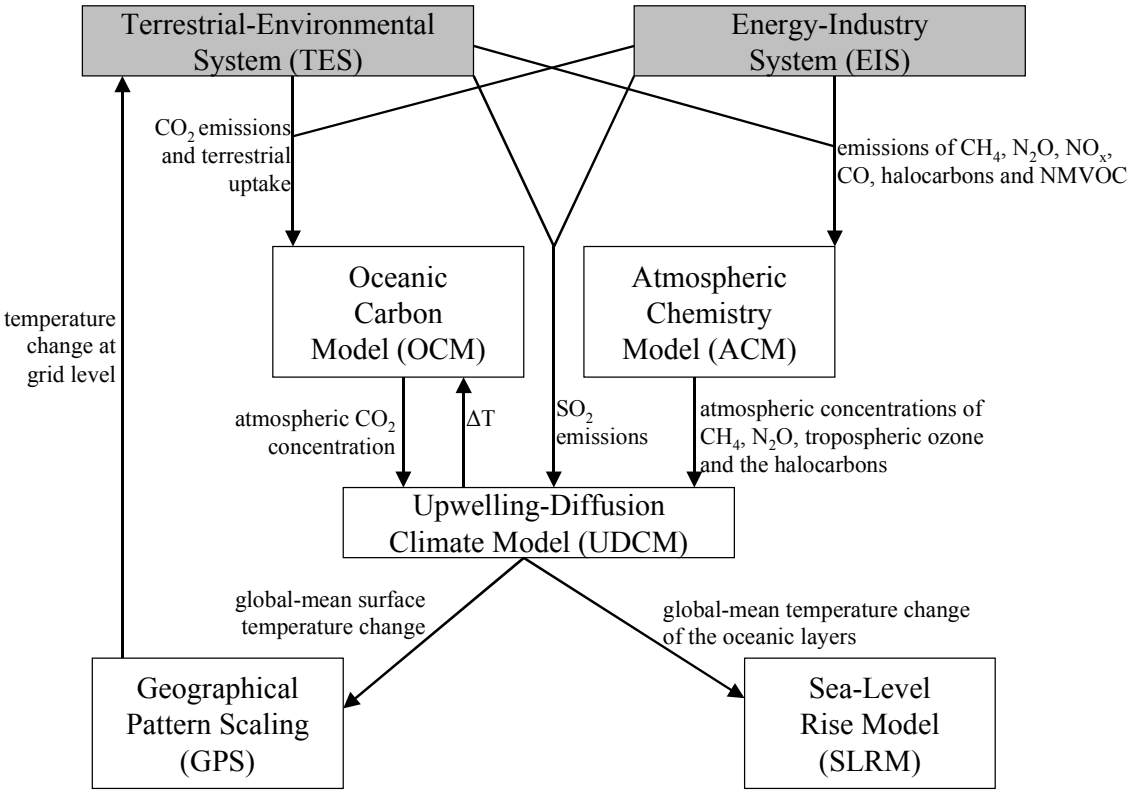

Figure 2.1 Flow diagram of the IMAGE 2.2. Atmosphere-Ocean System (AOS). The land-use and natural emissions (including terrestrial uptake of CO_2) from TES and energy and industry emissions from EIS represent the AOS input. Concentration changes, changes in radiative forcing, temperature changes and sea-level rise are outputs from AOS. The global-mean temperature change of the oceanic mixed layer is used as input for the oceanic carbon model.

2.2 Differences with AOS in IMAGE 2.1

The largest difference between the AOS in IMAGE 2.1 and IMAGE 2.2. is the latter's use of overall global-mean approach in comparison to the zonal approach of the climate and ocean model in IMAGE 2.0 and 2.1. In IMAGE 2.2, all calculations are done at a global level, except for the last step, in which the global temperature increase is scaled to a grid level by GPS. This development of a new global-mean approach was stimulated by the

[8] The sulphur patterns were kindly provided by Michael Schlesinger and Sergej Malyshev.

recommendations of the 3rd IMAGE-2 Advisory Board of IMAGE in November 1999 (Tinker et al., 2000), stating that:

'…
The current zonal-mean climate/ocean model should be replaced by a two-track approach in which both a simple climate/ocean model and a 3D atmosphere/ocean general circulation model (i.e., ECBilt) are used for appropriate purposes (respectively, uncertainty and land/climate interactions). …'

The main argument for this was that a two-dimensional approach of the climate system does not differ significantly from a one-dimensional approach. Hence, UDCM and OCM can replace the zonal-mean climate/ocean model as described in De Haan et al. (1994). The climate model, MAGICC (Hulme et al., 2000), is used as the basis for UDCM since it is has a widely accepted status in the scientific world and is well-known within the IPCC.

However, the zonal-mean climate/ocean model, IMAGE 2.1, couples the temperature change of the ocean with its carbon uptake. Because UDCM only calculates the temperature change of the ocean, we implemented OCM in IMAGE 2.2. The choice for the Bern Oceanic Carbon Cycle model was based on its use in the IPCC-TAR carbon cycle calculations. Because of the global-mean approach of our climate model, we had to replace the method of taking the non-linear effect of sulphate aerosols into account, as described in Alcamo et al. (1998). On the advice of the 3rd IMAGE-2 Advisory Board, we chose the method of Schlesinger et al. (2000).Finally, the calculations of the atmospheric concentrations (simulated by ACM) and the radiative forcings were updated according to the latest scientific literature as assessed in the TAR (IPCC, 2001).

All these changes and improvements of AOS in IMAGE 2.2 contribute to the possibility of using AOS in the FAIR modelling framework (Den Elzen and Lucas, 2003), because of the similar one-dimensional modelling philosophy (see Den Elzen and Schaeffer, 2002). The three-dimensional approach mentioned in the recommendation of the 3rd Advisory Board above will be explored in co-operation with the KNMI in the next version of IMAGE (i.e. IMAGE 3.0).

3. Modelling concentrations

How the concentration of the major greenhouse gas CO_2 is calculated is described in section 3.1, while the calculation of the concentrations of the other non-CO_2 greenhouse gases and other gases is described in section 3.2. For CO_2, only the oceanic uptake is explained in this report since the terrestrial processes concerning CO_2 form part of TES (see IMAGE team, 2001a). Hence, section 3.1 describes the Oceanic Carbon Model (OCM) and section 3.2, the Atmospheric Chemistry Model (ACM). For insight into the terrestrial carbon model of IMAGE 2.2, the reader is referred to Leemans et al. (2002).

3.1 Oceanic Carbon Model (OCM)

In the Oceanic Carbon Model (OCM) of IMAGE 2.2, the oceanic component of carbon is represented by a mathematical function (known as a convolution integral), which can be attuned to closely replicate the behaviour of more complex oceanic models. This approach is based on the Bern carbon cycle-climate (Bern CC) model developed at the Physics Institute of the University of Bern, Switzerland. The approach described by Joos et al. (1996) is based on the application of a mixed-layer pulse response function. The advantage of such a mixed-layer response function is that it is possible to represent the non-linear effects of seawater chemistry. This non-linearity occurs in the transition from CO_2 to HCO_3^- and CO_3^- when CO_2 dissolves in the ocean. Hence, a mixed-layer response function represents the time-dependent reaction of the ocean on changes in the atmospheric partial pressure of CO_2.

The model input and output variables of the OCM:

Model input	- CO_2 emissions from energy and industrial sources (modelled in EIS) - CO_2 emissions from land-use change (modelled in TES) - CO_2 uptake by full-grown forest (modelled in TES) - Global mean temperature change of the oceanic mixed layer (modelled in UDCM)
Model output	- Oceanic CO_2 uptake (output variable to complete the carbon cycle) - Atmospheric CO_2 concentration (used as input in UDCM)

Methodology

The global carbon balance can be expressed explicitly in a basic mass conservation equation:

$$\frac{\Delta[CO_2]}{\Delta t} = E_{\text{fos}} + E_{\text{land}} - S_{\text{ref}} - S_{\text{veg}} - S_{\text{oc}} \qquad (3.1)$$

where $\Delta[CO_2]/\Delta t$ is the change in atmospheric CO_2, E_{fos} the CO_2 emission from fossil fuel burning and industrial sources (cement production and chemical feedstocks), E_{land} the CO_2 emission from land-use changes (e.g. deforestation), S_{ref} the CO_2 uptake by regrowing vegetation (assumed to be an anthropogenic activity), S_{veg} the CO_2 uptake by full-grown vegetation (a natural process) and S_{oc} the CO_2 uptake by the oceans (all fluxes in Gt C per year).

The oceanic uptake of CO_2 is calculated each year, depending on the pressure difference between atmosphere and the ocean surface. The net air-to-sea flux F_{as} is calculated in the following equation:

$$F_{as} = K_g \left([CO_{2,a}] - [CO_{2,s}] \right) \qquad (3.2)$$

where K_g represents the global average gas exchange coefficient (9.06^{-1} years^{-1}) and [$CO_{2,a}$] and [$CO_{2,s}$] the global average partial pressure of CO_2 in the atmosphere and surface ocean, respectively (in ppmv).

The effect of the newly calculated air-to-sea flux on the perturbation in dissolved inorganic carbon is obtained from the convolution integral of the mixed layer response function r_s:

$$\delta\sum CO_2 = \frac{c}{h_m A_{ocean}} \int_{t_0}^{t} f_{as}(t') \cdot r_s(t-t')dt' \qquad (3.3)$$

where t_0 is the pre-industrial year, 1765, with a CO_2 concentration level of 278 ppmv, and t' is the previous time step. A_{ocean} represents the ocean area (3.62 x 10^{14} m^2), c, a unit conversion (1.722 x 10^{17} μmol m^3 ppm^{-1} kg^{-1}) and h_m the mixed layer depth (75 m). The mixed layer response function r_s is based on the High-Latitude Exchange/Interior Diffusion-Advection (HILDA) model of the University of Bern (Joos et al., 1996).

The perturbation in dissolved inorganic carbon has an effect on the perturbation in the sea surface partial pressure relative to the pre-industrial temperature, T_0, which is assumed to be 18.2 °C. In an equation:

$$\begin{aligned}\delta\left[CO_{2,s}\right]_{(T_0)} = \quad & \left(15.568 - 0.13993 \cdot T_0\right) \cdot 10^{-1} \cdot \left(\delta\sum CO_2\right) \\ & + \left(7.4706 - 0.20207 \cdot T_0\right) \cdot 10^{-3} \cdot \left(\delta\sum CO_2\right)^2 \\ & - \left(1.2748 - 0.12015 \cdot T_0\right) \cdot 10^{-5} \cdot \left(\delta\sum CO_2\right)^3 \\ & + \left(2.4491 - 0.12639 \cdot T_0\right) \cdot 10^{-7} \cdot \left(\delta\sum CO_2\right)^4 \\ & - \left(1.5468 - 0.15326 \cdot T_0\right) \cdot 10^{-10} \cdot \left(\delta\sum CO_2\right)^5\end{aligned} \qquad (3.4)$$

Finally, the CO_2 partial pressure increases exponentially with the sea surface temperature (see Takahashi et al., 1993). Consequently, the sea-surface partial pressure can be determined as below:

$$\left[CO_{2,s}\right](t) = \left(\left[CO_{2,s}\right](t_0) + \delta\left[CO_{2,s}\right]_{(T_0)}\right) \cdot \exp\left(0.0423 \cdot \Delta T(t)\right) \qquad (3.5)$$

where $\left[CO_{2,s}\right](t_0)$ is the pre-industrial sea surface pressure (assumed to be equal to the atmospheric pressure), and ΔT(t) the global mean sea surface temperature change of the oceanic mixed layer, calculated in UDCM (see Chapter 5).

The sea surface partial pressure in year t and the corresponding atmospheric partial pressure were calculated (see Equation 3.2) after several iterations in one year (Equations 3.2 to 3.5). The change in the atmospheric partial pressure determines the yearly net carbon flux, using the conversion 0.4688 ppmv*Pg^{-1} (Krol and Van der Woerd, 1994). For more information, the reader is referred to Joos et al. (1996), Joos et al. (1999) and Joos et al. (2001). An example of the FORTRAN code is given in Alfsen and Berntsen (1999).

Calibration

There are considerable uncertainties in our knowledge of the past and present sources and sinks of CO_2. The amount of carbon remaining in the atmosphere is the only well-known component of the budget. Logically, this parameter is used for the calibration of OCM. OCM

was given an initial year of 1765, explained by the slow response of oceans to changing atmospheric conditions. Consequently, the terrestrial carbon model of TES was also given the initial year of 1765. Besides these carbon cycle models of IMAGE, the upwelling-diffusion of climate and sea-level rise model were also placed in the period of 1765-1969 in which the agricultural land area (i.e. S_{ref} equals zero in Equation 3.1) was not expected to change. Hence, TES only calculates the terrestrial uptake of natural vegetation (S_{veg}) over this period. This uptake is varied due to historical climate conditions and atmospheric CO_2 concentration.

Data on energy and industry emissions (E_{fos}) are used as input (Marland and Boden, 2000) for the calibration period. Given the fact that the land-use emissions are the most uncertain factors of the carbon balance, we attuned the land-use emissions to reproduce the historical atmospheric concentrations (Keeling and Whorf, 2001). A comparison with other historical land-use emissions (Houghton et al., 1999) taught us that our land-use emissions are well within an uncertainty range, but somewhat on the lower side. As a final check, we compared IMAGE values assigned to the biomass pools and net primary production (NPP) per vegetation type (determining S_{veg}) with data from IPCC (2001). In Figure 3.1 we plotted the historical oceanic uptake, calculated by IMAGE 2.2 after the calibration, and compared the trend found with other more complex oceanic models.

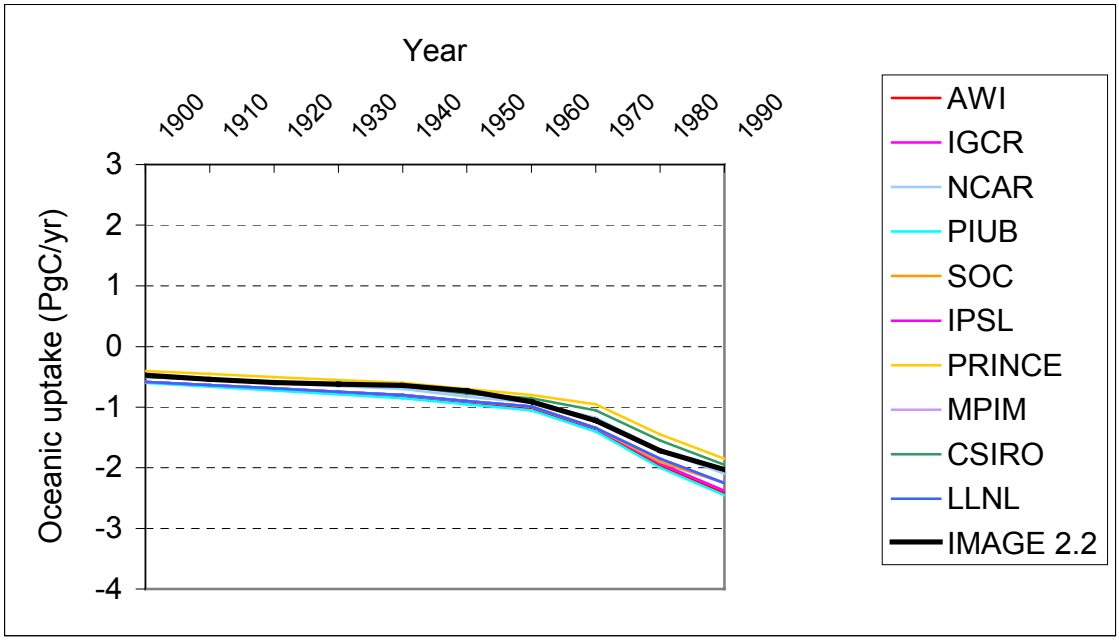

Figure 3.1 Net ocean uptake modelled by IMAGE 2.2 and 10 other more complex ocean models in Pg C per year. The other model results are taken from Figure 3.8, Third Assessment Report (IPCC, 2001). See the TAR for further details on these oceanic models.

From 1970 onward, IMAGE 2.2 simulates the complete society-biosphere-climate system, including land-use change. In Table 3.1, the different carbon fluxes for the 1980s and the 1990s from the literature are summarised (IPCC, 2001) and compared with the IMAGE 2.2 results (IMAGE team, 2001a). This calibration shows that IMAGE is well in line with measured data. The simulated slowdown of CO_2 emissions from deforestation during the 1990s is in line with the suggestion of IPCC (2001) that a slowdown in deforestation may have taken place in the early 1990s. Because abandoned grassland areas are replaced by the natural vegetation type (regrowing forest) in the land-cover model of IMAGE 2.2, there is an

increase in the carbon uptake. However, the completely increased negative land–atmosphere flux in IPCC (2001) cannot be reproduced by IMAGE 2.2. The reason for the increased terrestrial uptake is unclear; it may be caused by climate variability (not taken into account in IMAGE 2.2; see IPCC, 2001). Hence, the difference in the simulated land–atmosphere flux causes an oceanic uptake that does not decrease as in the data. These differences result in a net flux to the atmosphere that is larger than measured in the 1990s. The different fluxes for the 1980s are plotted in Figure 3.2.

Table 3.1 Carbon fluxes in the 1980s and 1990s as reported (IPCC, 2001) and calculated by IMAGE 2.2 (IMAGE team, 2001a)

Carbon fluxes (in GtC/yr)	1980s – IPCC	1980s – IMAGE 2.2	1990s – IPCC	1990s – IMAGE 2.2
Atmospheric increase	3.3 ± 0.1	3.5	3.2 ± 0.1	3.8
Emissions (fossil fuel, cement)	5.4 ± 0.3	5.65	6.3 ± 0.4	6.3
Ocean–atmosphere flux	-1.9 ± 0.6	-1.85	-1.7 ± 0.5	-2.1
Land–atmosphere flux	-0.2 ± 0.7	-0.3	-1.4 ± 0.7	-0.4
Partitioned as follows:				
• Land-use change[1)]	1.7 (0.6 to 2.5)	1.1	Insufficient data	1.2
• Residual terrestrial sink[2)]	-1.9 (-3.8 to 0.3)	-1.4	Insufficient data	-1.6

1) Land-use change in IMAGE 2.2 is determined by the emissions caused by deforestation due to agricultural expansion and influence of the timber industry, emissions caused by the use of traditional biomass as a fuel and emissions caused by decay of timber products (short-lived with lifetimes up to 10 years, e.g. paper and pulpwood; and long-lived with lifetimes up to 100 years, e.g. industrial roundwood for construction). The uptake by regrowth of forests after timber extraction or abandonment of agricultural land is subtracted from these land-use emissions to determine the CO_2 land-use emissions caused by anthropogenic activities.

2) The terrestrial sink calculated by IMAGE 2.2, as mentioned in this table, is the uptake by natural, full-grown vegetation, hence, mainly determined by the fertilization effect.

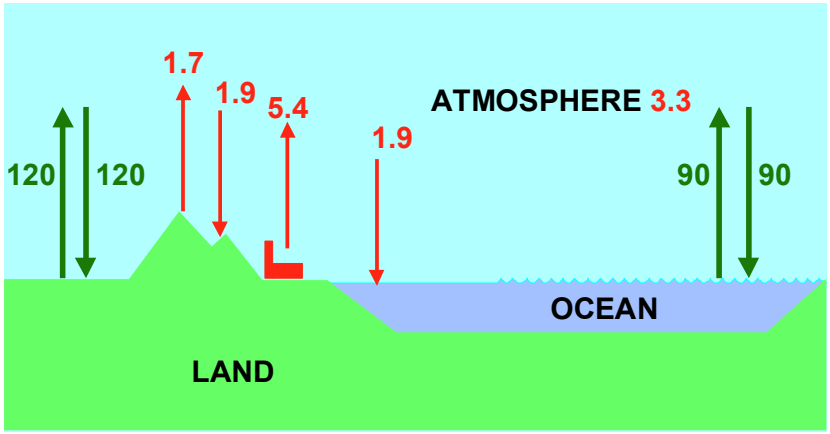

Figure 3.2: Visualisation of the carbon fluxes between land, atmosphere and ocean. The green arrows represent natural fluxes in equilibrium. The red arrows represent the carbon fluxes as a consequence of anthropogenic disturbance. The values, valid for the 1980s) (see Table 3.1) are taken from IPCC (2001).

IPCC SRES projections

Figure 3.3 shows how the oceanic fluxes follow the net atmospheric fluxes: a large increase in the net flux because of increasing energy emissions and deforestation fluxes (A2) is partly

compensated by an increased uptake flux of carbon into the ocean. On the other hand, the figure shows a lower oceanic uptake in the B1 world, where the net flux declines because of a decreasing population focused on sustainable development. The resulting CO_2 concentration profiles are depicted in Figure 3.4.

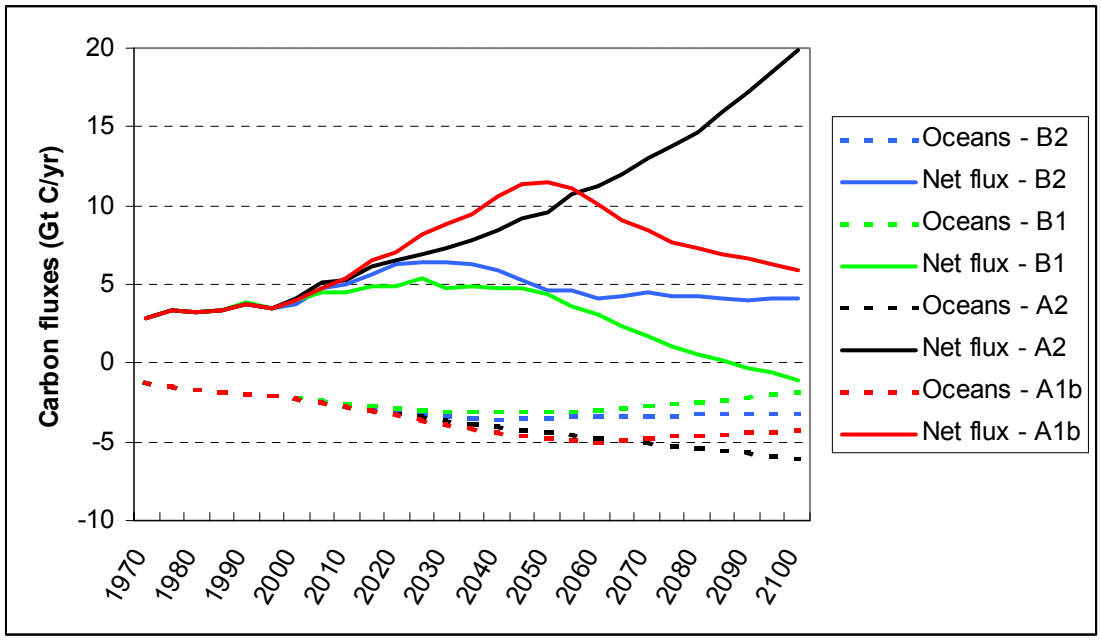

Figure 3.3: Two carbon fluxes for each SRES scenario (IPCC, 2000): the oceanic uptake and the net flux in Gt C per year. Results are taken from IMAGE team (2001a).

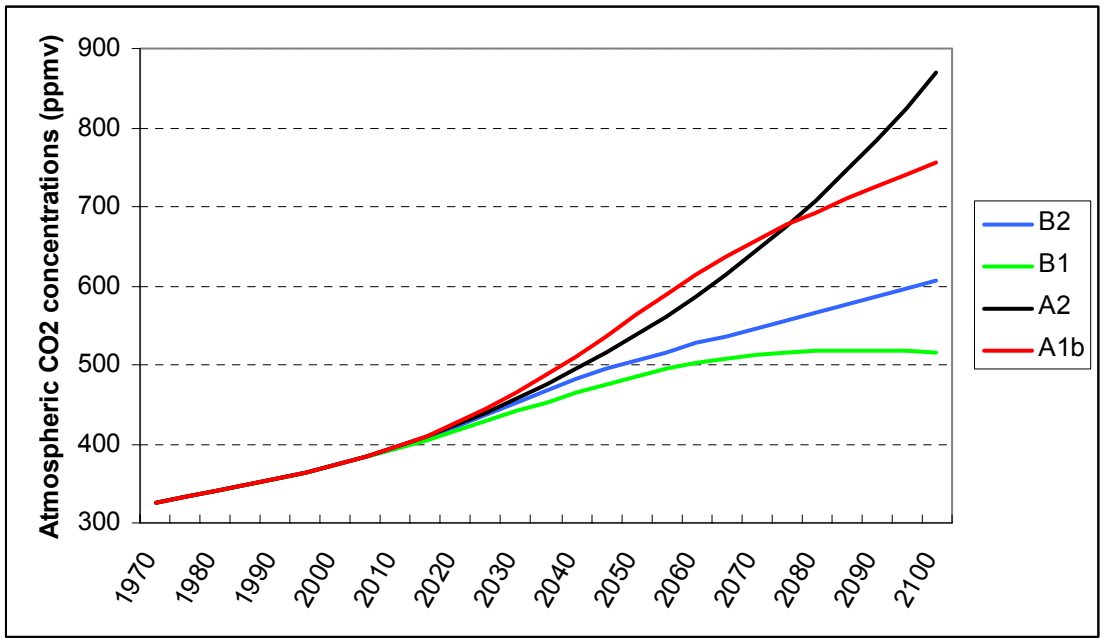

Figure 3.4: The atmospheric CO_2 concentrations for the SRES scenarios (IPCC, 2000) as implemented by the IMAGE 2.2 model (IMAGE team, 2001a).

3.2 Atmospheric Chemistry Model (ACM)

The Atmospheric Chemistry Model (ACM) calculates the global-mean atmospheric concentrations of the most important non-CO_2 greenhouse gases and ozone precursors. All the model input and output variables of ACM are listed below:

Model input	- Land-use and natural emissions of CH_4, N_2O, NO_x, CO and NMVOC (from TES) - Energy and industry emissions of CH_4, N_2O, NO_x, CO, NMVOC and the halocarbons (from EIS)
Model output	- Concentrations of CH_4, N_2O, tropospheric ozone and halocarbons (used as input in UDCM) - Concentrations of CO and the OH-radical - Chemical and atmospheric lifetime of CH_4

The first version of ACM was developed by Krol and Van der Woerd (1994). An extensive sensitivity analysis with the model, as described in Eickhout (1999), showed that ACM did not give good results in more extreme scenarios. Figure 3.5 shows that the ACM versions in IMAGE 2.0 and 2.1 even needed a ceiling for the OH concentrations; otherwise, the OH concentrations would increase too fast. The reason for this very reactive result of IMAGE 2.0/2.1 lies within a chain of chemical reactions of NO_x, CO and CH_4 that is too interlinked and so leads to too much mutual strengthening. For further information on the shortcomings of AOS-IMAGE 2.0/2.1, the reader is referred to Eickhout (1999). The new version of AOS is explained below.

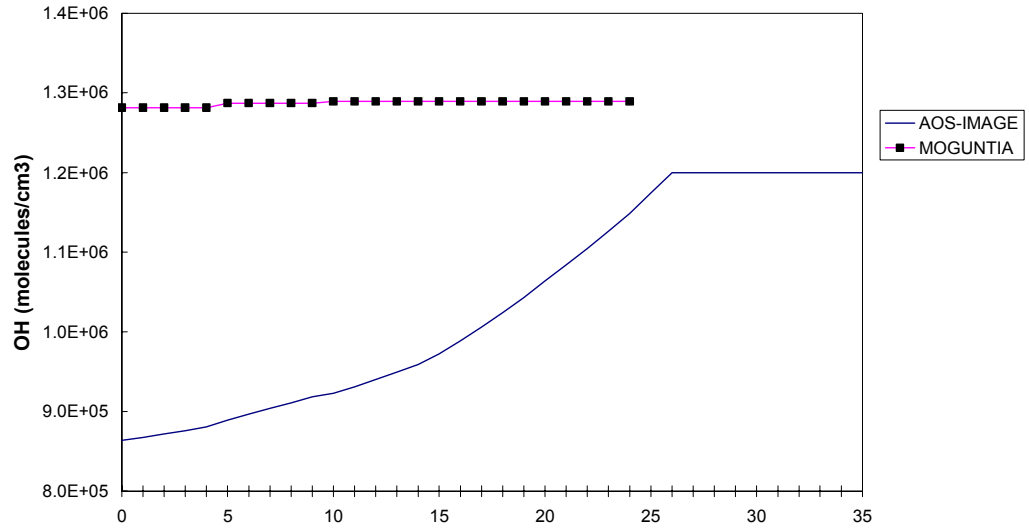

Figure 3.5: Comparison of a sensitivity run by AOS-IMAGE 2.0/2.1 and the three-dimensional global chemistry model, MOGUNTIA (introduced by Zimmerman, 1988 and further developed by The, 1997). In this sensitivity run the CH_4 and CO emissions are kept constant, and the emissions of NO_x and NMVOC are increased by 1% per year for over a period of 35 years. The different absolute values in the first year are introduced by different model settings. For further information on these sensitivity runs, the reader is referred to Eickhout (1999).

Methodology
Except for N_2O and the CFCs, the non-CO_2 greenhouse gases are not as inert as CO_2. Consequently, the different gases are closely linked to each other and the change in concentration of one gas influences the change in concentration of another gas. This dependency is seeking an elegant means to model the intermolecular dependencies and, at the same time, keep computation time within acceptable limits. The modelling methodology is explained below.

CH_4, N_2O and halocarbons
The emissions of the greenhouse gas and its subsequent removal from the atmosphere determine the concentration. The lifetime of a greenhouse gas indicates the efficiency of the removal process and is a measure of the time that passes before an emission pulse is removed from the atmosphere. For methane (CH_4), nitrogenous oxide (N_2O) and the halocarbons (including SF_6), the rate of removal is linearly dependent on the concentration of the compound, and is derived by multiplying the concentration by the lifetime factor, as adopted in most current IPCC simple climate models (Harvey et al., 1997). The rate of change for the concentration is then expressed as:

$$\frac{\Delta[GHG]}{\Delta t} = cv_{GHG} \cdot E_{GHG} - \frac{[GHG]}{\tau_{GHG}} \qquad (3.6)$$

where ΔGHG is the atmospheric concentration of greenhouse gas GHG, E_{GHG} the total emissions, τ_{GHG} the atmospheric exponential decay time or lifetime (yr) and cv_{GHG} a mass-to-concentration conversion factor. The lifetime of nitrous dioxide (N_2O) and most halocarbons (except for the partial chlorinated halocarbons: HCFCs, HFCs and CH_3CCl_3; see Table 3.2) is assumed to be constant because of the inertness of these gases.

Table 3.2: Atmospheric lifetimes of the most important greenhouse gases assumed to be inert in the troposphere (constant lifetime), as adopted in IMAGE 2.2. Source: IPCC, 2001

Greenhouse gases with constant lifetimes	*Lifetime (in years)*
N_2O	120.0
CFC-11	45.0
CFC-12	100.0
CFC-113	85.0
CFC-114	300.0
CFC-115	1700.0
CCl_4	35.0
Halon-1211	11.0
Halon-1301	65.0
CH_3Br	0.7
CF_4	50000.0
C_2F_6	10000.0
SF_6	3200.0

Because of the reactivity of the greenhouse gases, CH_4, HCFCs, HFCs and CH_3CCl_3 with the OH radical, the atmospheric lifetimes of these gases cannot be assumed to be constant. The OH abundance for these compounds is also taken into account. Hence, the atmospheric lifetime in Equation 3.7 is calculated as:

$$1/\tau_{GHG} = 1/\tau_{chemical} + 1/\tau_{stratospheric} + 1/\tau_{soil-loss} \quad (3.7)$$

where: τ_{GHG} = atmospheric lifetime of greenhouse gas *GHG* (i.e. CH_4, HCFCs, HFCs and CH_3CCl_3: in years);
$\tau_{chemical}$ = chemical lifetime of the same greenhouse gas (in years);
$\tau_{stratospheric}$ = lifetime due to loss to stratosphere (in years);
$\tau_{soil\text{-}loss}$ = lifetime due to loss to biosphere (soil; in years).

The lifetimes due to losses to the stratosphere and the biosphere are assumed constant. The chemical lifetime of these greenhouse gases is determined by the reaction rate for the oxidation by OH radicals (assuming a one-order reaction):

$$\tau_{chemical} = \frac{1}{k_{GHG+OH} * [OH]} \quad (3.8)$$

with:

k_{GHG+OH} = reaction rate (cm^3 per year)
$[OH]$ = OH concentration (molecules per cm^3)

Hence, the abundance of the OH radical in the troposphere determines the chemical lifetime of the reactive tracers, and therefore the atmospheric lifetime (Equation 3.7) and the atmospheric concentration (Equation 3.6).

The OH radical plays an important role in the tropospheric chemistry because of its reactivity. Equation 3.9 shows that the OH radical is involved in a set of reactions with, in this case, methane and CO. Methane can be replaced by all other non-methane volatile organic compounds (NMVOCs).

$$\begin{aligned} &CO + OH\cdot \rightarrow CO_2 + H\cdot \\ &H\cdot + O_2 \rightarrow HO_2\cdot \\ &CH_4 + OH\cdot \rightarrow CH_3\cdot + H_2O \\ &CH_3\cdot + O_2 \rightarrow CH_3O_2\cdot \end{aligned} \quad (3.9)$$

Furthermore, the presence of NO_x determines whether more radicals are formed or depleted. In the absence of NO_x, fewer radicals can be formed and less tropospheric ozone depleted (Equation 3.10); in the presence of NO_x more radicals and tropospheric ozone can be formed (Equation 3.11).

$$\begin{aligned} &CH_3O_2\cdot \text{ or } HO_2\cdot + O_3 \rightarrow 2O_2 + CH_3O\cdot \text{ or } OH\cdot \\ &CH_3O_2\cdot \text{ or } HO_2\cdot + OH\cdot \rightarrow O_2 + CH_3OH \text{ or } H_2O \end{aligned} \quad (3.10)$$

$$\begin{aligned} &CH_3O_2\cdot \text{ or } HO_2\cdot + NO \rightarrow NO_2 + CH_3O\cdot \text{ or } OH\cdot \\ &NO_2 + h\nu(\lambda \leq 410nm) \rightarrow NO + O\cdot \\ &O\cdot + O_2 \rightarrow O_3 \end{aligned} \quad (3.11)$$

This complex reaction scheme represents only a small part of the many reactions with OH occurring in the troposphere. In IMAGE 2.2, the OH abundance is calculated with use of sensitivity coefficients for reactions of OH with CH_4, CO, NO_x and NMVOC. This approach is based on the OxComp experiment, developed to calculate the atmospheric concentrations of the most important reactive gases, given the SRES scenarios (IPCC, 2001). In this approach, simple parameterisations are determined by re-simulating the results of complex three-dimensional atmospheric chemistry models of one SRES run. Although the resulting parameterisation of the complex tropospheric chemistry has been very simplified (see Equation 3.12), it gives a good idea of the concentration change in the OH radical expected in the future. However, note that the approach neglects the possible impact of climate change on the tropospheric chemistry.

$$\Delta \ln[OH] = R_{CH_4} \cdot \Delta \ln[CH_4] + R_{NO_x} \cdot \Delta E_{NO_x} + R_{CO} \cdot \Delta E_{CO} + R_{NMVOC} \cdot \Delta E_{NMVOC} \quad (3.12)$$

where R_{gas} stands for the sensitivity coefficient of each reactive gas (see Table 3.3).

Table 3.3: Sensitivity coefficients to determine the change of OH abundance and tropospheric ozone concentration, as shown in Equations 3.12 and 3.14.

Sensitivity coefficient	*In relation to the OH radical (Equation 3.12)*	*In relation to tropospheric ozone (Equation 3.14)*
R_{CH4}	-0.32	6.7
R_{NOx}	0.0042	0.17
R_{CO}	-0.000105	0.0014
R_{NMVOC}	-0.000315	0.0042

Note: Values are based on the OxComp experiment (IPCC, 2001).

This sensitivity coefficient determines the OH abundance, depending on the increase in the four mentioned reactive gases. Table 3.3 shows the OH abundance to decline by 0.32% for every 1% increase in CH_4. This sensitivity coefficient is also called the chemical feedback parameter.

With the calculated OH abundance from Equation 3.12, the concentrations of CH_4, HCFCs, HFCs and CH_3CCl_3 can be calculated. For these calculations, the lifetimes due to losses to the stratosphere and biosphere (Equation 3.7) plus the reaction rate (Equation 3.8) need to be known. In Table 3.4 these fixed values are summarised (based on Krol and Van der Woerd, 1994 and IPCC, 2001).

Table 3.4: Reaction rates and transport losses of greenhouse gases that react with the OH radical (CH_4, HCFCs, HFCs and CH_3CCl_3) and taken into account by IMAGE 2.2.

Greenhouse gas taken into account by IMAGE 2.2	*Reaction rate of the oxidation by OH (in cm^3/yr)*	*Transport losses to stratosphere and biosphere (yr^{-1})*
CH_4	$1.274 \cdot 10^{-7}$	0.0063
CH_3CCl_3	$1.781 \cdot 10^{-7}$	0.0213
CH_3Cl	$9.101 \cdot 10^{-7}$	0.02
HCFC-22	$8.482 \cdot 10^{-8}$	0.0042
HCFC-123	$8.150 \cdot 10^{-7}$	0.0213
HCFC-124	$1.985 \cdot 10^{-7}$	0.0078
HCFC-141b	$1.144 \cdot 10^{-7}$	0.0132
HCFC-142b	$5.773 \cdot 10^{-8}$	0.0046
HCFC-225ca	$1.683 \cdot 10^{-7}$	0.0083
HFC-23	$4.640 \cdot 10^{-9}$	0.0
HFC-32	$1.930 \cdot 10^{-7}$	0.0
HFC-43-10-mee	$9.236 \cdot 10^{-8}$	0.0
HFC-125	$3.552 \cdot 10^{-8}$	0.0
HFC-134a	$9.236 \cdot 10^{-8}$	0.0
HFC-143a	$2.110 \cdot 10^{-8}$	0.0
HFC-152a	$8.044 \cdot 10^{-7}$	0.0
HFC-227ea	$2.830 \cdot 10^{-8}$	0.0
HFC-236fa	$4.640 \cdot 10^{-9}$	0.0
HFC-245ca	$1.660 \cdot 10^{-7}$	0.0

Note: For CH_4, the respective transport losses to stratosphere and biosphere were determined at 1/120 and 1/160. These values are taken from Krol and Van der Woerd (1994) and IPCC (2001).

Tropospheric ozone (O_3)
As already shown, the tropospheric ozone concentration is very much connected to the OH abundance. Some further reactions are given in the following scheme:

$$\begin{aligned} &O_3 + h\nu(\lambda \le 310nm) \rightarrow O\cdot + O_2 \\ &O\cdot + O_2 \rightarrow O_3 \\ &O\cdot + H_2O \rightarrow 2OH\cdot \end{aligned} \qquad (3.13)$$

Hence, the determination of tropospheric ozone is very similar to the determination of the OH abundance. Again, this approach is based on the OxComp experiment in IPCC (2001). See Table 3.3 for the values in Equation 3.14.

$$\Delta \ln[trop.O_3] = R_{CH_4} \cdot \Delta \ln[CH_4] + R_{NO_x} \cdot \Delta E_{NO_x} + R_{CO} \cdot \Delta E_{CO} + R_{NMVOC} \cdot \Delta E_{NMVOC} \qquad (3.14)$$

In this way ACM is still globally averaged, but the shortcomings of AOS-IMAGE 2.0/2.1 (Eickhout, 1999) are removed.

The determination of the CO concentration has not changed since Krol and Van der Woerd (1994).

Calibration
Given the historical emissions from EIS and the calibrated emissions from TES, ACM is compared with historical data for N_2O (Figure 3.6) and CH_4 (Figure 3.7). Until 1990 IMAGE 2.2 was very capable of following the historical data.

For methane (CH_4) IMAGE follows the measured data very well until 1990. However, after 1990 some differences are very clear. For CH_4 the decrease of methane in the 1990s cannot be reproduced by IMAGE 2.2. However, the decline in the methane yearly growth rate after 1991 has been topic of great discussion. One of the hypotheses is that the Pinatubo eruption in 1991 caused a decrease in stratospheric ozone and therefore an increase in UV in the troposphere. An increase in UV would increase the OH abundance and therefore the decrease in methane. Since IMAGE 2.2 uses constant vulcano emissions, this extreme event cannot be reproduced by ACM.

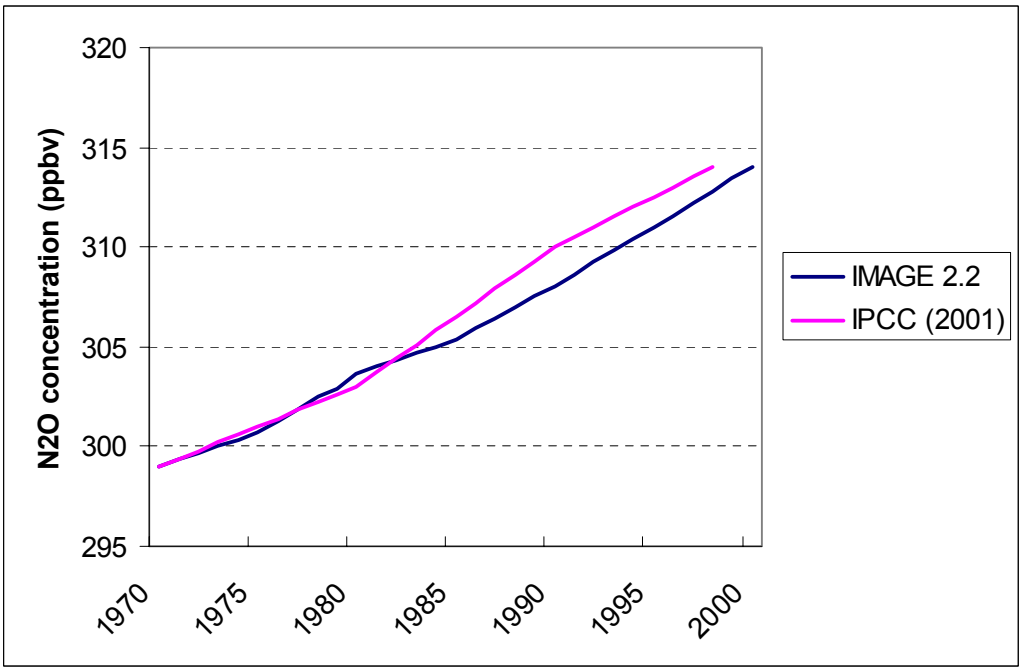

Figure 3.6: Historical N_2O concentration in ppbv; IMAGE 2.2 results compared with data (IPCC, 2001).

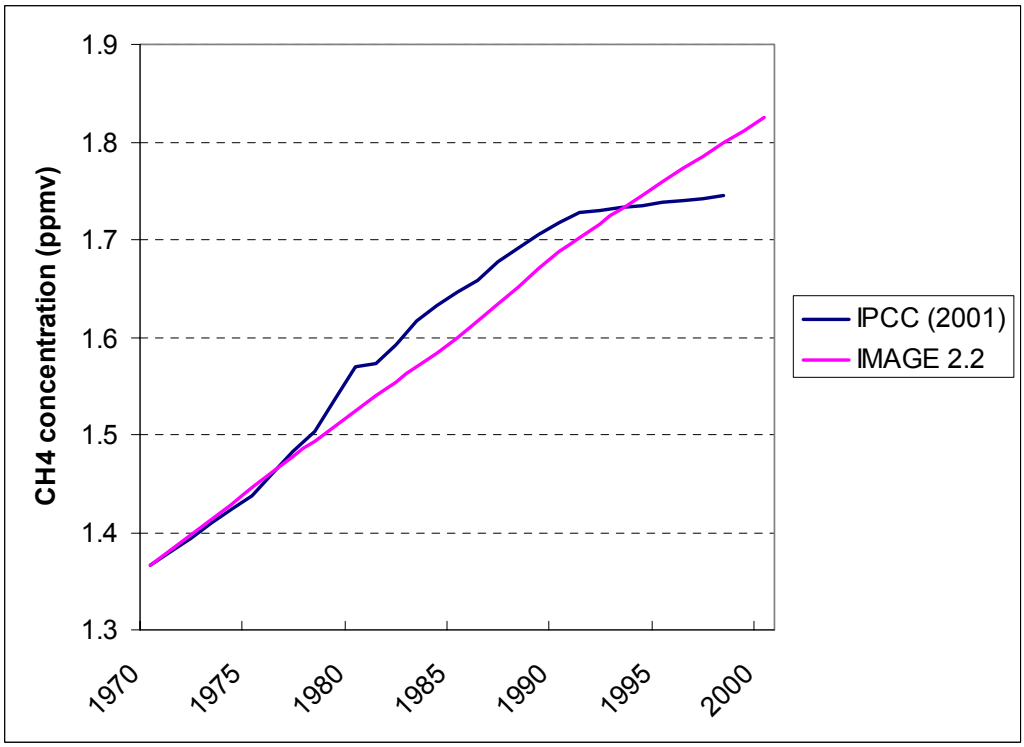

Figure 3.7: Historical CH_4 concentration in ppmv; IMAGE 2.2 results compared with data (IPCC, 2001).

IPCC SRES projections

Figures 3.8 and 3.9 show the SRES projections as implemented by IMAGE 2.2 (IMAGE team, 2001a). Again the A2 and B1 scenario span up the SRES range by the end of the 21st century.

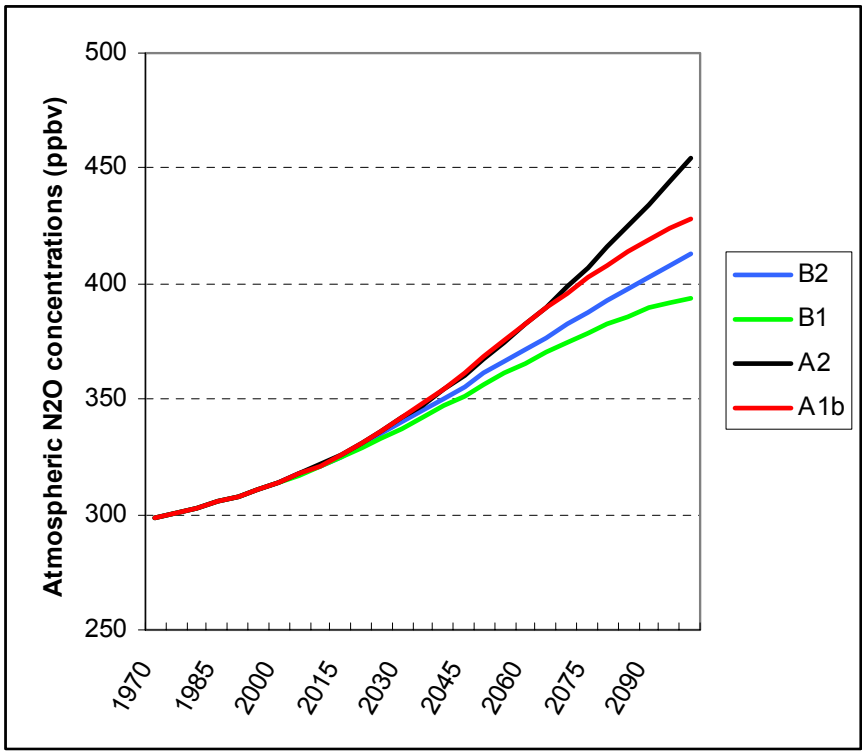

Figure 3.8: Atmospheric concentrations for N_2O for the SRES scenarios (IPCC, 2000) as implemented by the IMAGE 2.2 model (IMAGE team, 2001a).

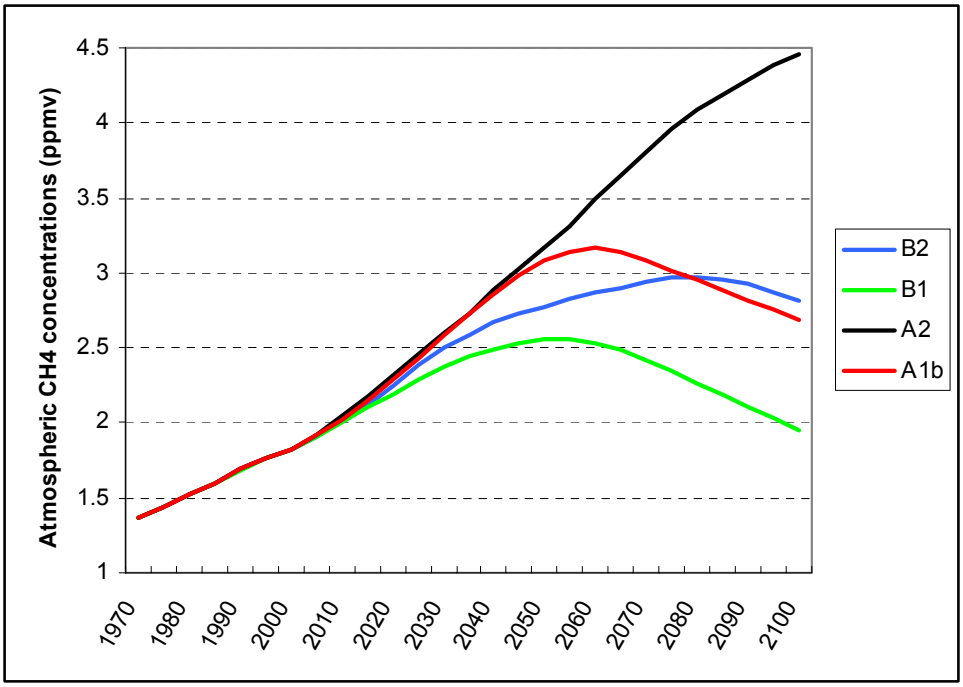

Figure 3.9: Atmospheric concentrations for CH_4 for the SRES scenarios (IPCC, 2000) as implemented by the IMAGE 2.2 model (IMAGE team, 2001a).

4. Modelling radiative forcing

Increased concentrations of greenhouse gases in the atmosphere lead to a change in radiative forcing, a measure of the extra energy input to the surface-troposphere system. This increased radiative forcing leads to an increase in the global-mean surface temperature. The radiative forcing calculations are fully based on the latest scientific literature as assessed in the TAR (IPCC, 2001). This chapter presents the methodology, calibration and the SRES projections of the radiative forcing calculations by IMAGE 2.2, which is part of the Upwelling-Diffusion Climate Model (UDCM; see Figure 2.1).

4.1 Methodology

The methodology for determining the radiative forcings is given outlined in his section. The input and output of this AOS is given in the textbox below.

Model input	- Atmospheric concentrations of the most important greenhouse gases (CO_2, CH_4, N_2O, tropospheric O_3, CFCs, HCFCs, PFCs, Halon-1211, Halon-1301, CH_3Br, SF_6, CH_3CCl_3 and CH_3Cl (modelled in OCM and ACM; see Chapter 3). - Energy and land-use emissions of SO_2 (modelled in EIS and TES).
Model output	- Changes in radiative forcing for CO_2, CH_4, N_2O, tropospheric O_3, stratospheric O_3, CFCs, HCFCs, PFCs, Halon-1211, Halon-1301, CH_3Br, SF_6, CH_3CCl_3, CH_3Cl, stratospheric water vapour and a number of tropopsheric aerosols (used as input for UDCM).

CO_2

The radiative forcing of carbon dioxide is calculated as:

$$\Delta Q_{CO_2,t} = 5.325 \cdot \ln\left(\frac{[CO_2]_t}{[CO_2]_{t_0}}\right) \qquad (4.1)$$

where t_0 is 1765, the year of initialisation in IMAGE 2.2 (see section 3.1). The pre-industrial concentration of CO_2 is assumed to be 278 ppmv.

The value, 5.325, is based on the fact that doubling of the CO_2 concentration will lead to an increased forcing of 3.7 Wm^{-2}. This is in line with the assumed value given by IPCC (2001).

CH_4 and N_2O

As the concentration of a greenhouse gas increases, the forcing will gradually 'saturate' into certain absorption bands. An additional unit increase in concentration will gradually have a relatively smaller impact on radiative forcing. At present-day concentrations, the saturation effect is greatest for CO_2 and somewhat less for CH_4 and N_2O.

Additionally, some greenhouse gases absorb radiation in each other's frequency domains. This 'overlap effect' is especially relevant for CH_4 and N_2O. Increases in CH_4 concentration decrease the efficiency of N_2O absorption and vice versa. IMAGE 2.2 uses the following equations for taking this mechanism into account (IPCC, 2001):

$$\Delta Q_{CH_4,t} = 0.036 \cdot \left(\sqrt{[CH_4]_t} - \sqrt{[CH_4]_{t_0}}\right) - \left(0.47 \cdot \ln\left[\begin{array}{l} 1 + a \cdot \left([CH_4]_t \cdot [N_2O]_{t_0}\right)^{0.75} + \\ b \cdot [CH_4]_t \left([CH_4]_t \cdot [N_2O]_{t_0}\right)^{1.52} \end{array} \right] - 0.47 \cdot \ln\left[\begin{array}{l} 1 + a \cdot \left([CH_4]_{t_0} \cdot [N_2O]_{t_0}\right)^{0.75} + \\ b \cdot [CH_4]_{t_0} \left([CH_4]_{t_0} \cdot [N_2O]_{t_0}\right)^{1.52} \end{array} \right] \right) \quad (4.2)$$

for the change into radiative forcing of methane, and:

$$\Delta Q_{N_2O,t} = 0.12 \cdot \left(\sqrt{[N_2O]_t} - \sqrt{[N_2O]_{t_0}}\right) - \left(0.47 \cdot \ln\left[\begin{array}{l} 1 + a \cdot \left([CH_4]_{t_0} \cdot [N_2O]_t\right)^{0.75} + \\ b \cdot [CH_4]_{t_0} \left([CH_4]_{t_0} \cdot [N_2O]_t\right)^{1.52} \end{array} \right] - 0.47 \cdot \ln\left[\begin{array}{l} 1 + a \cdot \left([CH_4]_{t_0} \cdot [N_2O]_{t_0}\right)^{0.75} + \\ b \cdot [CH_4]_{t_0} \left([CH_4]_{t_0} \cdot [N_2O]_{t_0}\right)^{1.52} \end{array} \right] \right) \quad (4.3)$$

for the change into radiative forcing of nitrous oxide. The pre-industrial concentrations $[CH_4]_{t_0}$ and $[N_2O]_{t_0}$ are assumed to be 700 and 270 ppbv, respectively (IPCC, 2001). The values *a* and *b* are 2.01 x 10^{-5} and 5.31 x 10^{-15}, respectively.

Tropospheric ozone (O_3), halocarbons and SF_6

These greenhouse gases are calculated by using the tropospheric concentrations (calculated in ACM; see section 3.2) multiplied by the so-called radiative efficiency coefficients taken from IPCC (2001). Table 4.1 contains the radiative efficiency coefficients used in IMAGE 2.2.

Stratospheric ozone

Chlorinated and brominated halocarbons can lead to significant indirect forcing by the depletion of stratospheric ozone. This indirect forcing effect of some of the halocarbons is taken into account in IMAGE 2.2. However, the indirect effect of increasing UV field in the troposphere is not taken into account in IMAGE 2.2. An increase in UV because of less stratospheric ozone leads to an increase in OH and hence, an increased atmospheric decay of other greenhouse gases (methane). This effect is very difficult to quantify, especially since the ozone depletion is highly dependent on the altitude profile of the ozone loss. Therefore, only the forcing due to loss of stratospheric ozone is quantified in IMAGE 2.2. The following equation is used for this effect (Harvey et al., 1997):

$$\Delta Q_{strat.O_3,t} = -0.001 \times \left[0.000552 \sum \left(\left\{NCl_i \cdot C_{i,t}\right\}^{1.7}\right) + 3.048 \sum \left(NBr_i C_{i,t}\right)\right] \quad (4.4)$$

where C_i is the concentration in pptv of chlorinated or brominated halocarbon *i* and NCl_i and NBr_i are the number of chlorine or bromine atoms in compound *i*. In Table 4.1, the number of chlorine or bromine atoms are summed for the ozone-depleting compounds taken into account.

Stratospheric water vapour
The oxidation of methane produces water vapour that can contribute significantly to changes in stratospheric water vapour, which in itself, also leads to a radiative forcing. However, so far not much is known about the processes contributing to this forcing. In IMAGE 2.2, the indirect effect of methane oxidation is taken into account by the following equation (Harvey et al., 1997):

$$\Delta Q_{strat.H_2O,t} = 0.05 \cdot \Delta Q_{CH_4-direct,t} = 0.05 \cdot 0.036 \cdot \left(\sqrt{[CH_4]_t} - \sqrt{[CH_4]_{1765}}\right) \qquad (4.5)$$

Direct radiative forcing of tropospheric aerosols
In IMAGE 2.2, only the direct effects of the sulphate, fossil fuel black carbon, fossil fuel organic carbon and biomass burning aerosols are taken into account. Other tropospheric aerosols such as mineral dust aerosols and nitrate aerosols are not considered. IPCC (2001) estimates the effect of mineral dust aerosols from –0.60 to 0.40 W/m^2. Given the lack of scientific information on nitrate aerosols "best estimates" are not given.

The direct effect of aerosols is caused by scattering and absorbing short-wave and long-wave radiation with a resulting perturbation of the energy budget of the Earth/atmospheric system. In simple climate models (SCMs) the direct component of the forcing is assumed to vary linearly with concentration and hence with emissions. In an equation for the effect of sulphate aerosols (Harvey et al., 1997):

$$\Delta Q_{SO_4-direct,t} = \frac{emis_{SO_2,t}}{emis_{SO_2,1990}} \cdot \Delta Q_{SO_4-direct,1990} \qquad (4.6)$$

where forcing in 1990 is assumed to be -0.3 W/m^2. Note that only the anthropogenic emissions due to energy use and industrial activities are considered in this equation. The 1990 emissions within IMAGE 2.2, are assumed to be 71.6 Tg S (Olivier et al., 1996).

For fossil fuel, black and organic carbon aerosols, the same approach as for sulphate aerosols is chosen, since these aerosols are also formed due to anthropogenic energy and industrial emissions. Note that soot decreases the reflection and thus, increases the absorption of solar radiation. The 1990 level of the combination of black and organic carbons is assumed to be 0.1 W/m^2 (IPCC, 2001).

The same approach is used again for biomass burning aerosols. However, scaling for these aerosols is performed using the change in SO_2 emissions due to land-use change. In 1990, the land-use emissions are 1.75 Tg S (IMAGE team, 2001a), while the forcing in 1990 due to biomass burning aerosols is assumed to be –0.2 W/m^2 (IPCC, 2001).

Indirect radiative forcing of tropospheric aerosols
Aerosols serve both as cloud condensation and ice nuclei. As a result, the aerosols change the microphysics, the radiative properties and the lifetime of clouds, and hence, change the cloud albedo and amount. This effect is called the indirect radiative forcing caused by aerosols. Moreover, there are two indirect effects to distinguish: 1) an increase in aerosols, causing an increase in droplet concentration, and 2) the reduction in cloud droplet size, affecting the precipitation efficiency and tending to increase the liquid water content, the cloud lifetime and the cloud thickness (IPCC, 2001). Because of the many uncertainties, it is very difficult to quantify these indirect effects. A few factors that may contribute to this uncertainty are:

- that pre-industrial sulphate varies by a factor of just over 2;
- that the variance in the industrial sulphate concentrations is about 50%;
- that the parameterizations of relating droplet number concentration to aerosol concentration are very uncertain;
- that changes in the vertical distribution of the aerosol will affect the indirect forcing because of changes in its spatial relationship to cloud (IPCC, 2001).

Table 4.1: Radiative efficiency coefficients in IMAGE 2.2 based on IPCC (2001)[3)]

Chemical compound	*Radiative efficiency coefficient (in $W*m^{-2}*ppbv^{-1}$)*	*Number of chlorine or bromine atoms per compound*
Tropospheric ozone[1)]	0.042[2)]	0
CFC-11	0.25	3
CFC-12	0.32	2
CFC-113	0.30	3
CFC-114	0.31	2
CFC-115	0.18	1
CCl_4	0.13	4
CH_3CCl_3	0.06	3
CH_3Cl[1)]	0.01	1
HCFC-22	0.20	1
HCFC-123	0.20	2
HCFC-124	0.22	1
HCFC-141b	0.14	2
HCFC-142b	0.20	1
HCFC-225ca	0.27	2
HFC-23	0.16	0
HFC-32	0.09	0
HFC-43-10-mee	0.40	0
HFC-125	0.23	0
HFC-134a	0.15	0
HFC-143a	0.13	0
HFC-152a	0.09	0
HFC-227ea	0.30	0
HFC-236fa	0.28	0
HFC-245ca	0.23	0
Halon-1211	0.30	1
Halon-1301	0.32	1
CH_3Br[1)]	0.01	1[4)]
CF_4[1)]	0.08	0
C_2F_6	0.26	0
SF_6	0.52	0

1) The pre-industrial concentration of natural occurring greenhouse gases is subtracted before the multiplication by the radiative efficiency coefficient to obtain the radiative forcing compared to pre-industrial times. Pre-industrial concentrations are 25.0 DU (Dobson Unit) for tropospheric ozone, 600 ppbv for CH_3Cl, 4.1ppbv for CH_3Br and 40ppbv for CF_4.

2) The unit of the radiative efficiency coefficient for ozone is $W*m^{-2}*DU^{-1}$.

3) The values for the halocarbons and SF_6 are taken from Table 6.7 and for O_3 from Table 6.3.

4) Due to the short lifetime of CH_3Br, the bromine atom is not considered to deplete stratospheric ozone.

Within IMAGE 2.2, only the first indirect effect of sulphate aerosols is taken into account. Indirect radiative forcings by carbonaceous aerosols, mineral dust aerosols and gas-phase nitric acid are rarely assessed. Hence, IMAGE 2.2 cannot quantify these effects. For the indirect effect of sulphate aerosols, IMAGE 2.2 uses the equation according to Harvey et al. (1997):

$$\Delta Q_{SO_4-indirect,t} = \frac{\log\left(1+{emis_{SO_2,t}}/{emis_{SO_2-nat}}\right)}{\log\left(1+{emis_{SO_2,1990}}/{emis_{SO_2-nat}}\right)} \cdot \Delta Q_{SO_4-indirect,1990} \qquad (4.7)$$

where the indirect forcing in 1990 is assumed to be –0.8 W/m^2. The natural emissions are mainly volcanoes and dimethyl sulphide (by oceans, land biota and soils). These emissions are difficult to quantify. IMAGE 2.2 uses a constant amount of 34.4 Tg S per year and well within the range of the IPCC (2001): 18-62 Tg S per year.

Note that because of the logarithm dependence of the indirect effect, the direct effect of sulphate aerosols becomes relatively larger when the sulphate aerosol loading increases.

Forcings not taken into account
Besides the forcings already mentioned, the following forcings are not taken into account either by IMAGE 2.2: the forcing by stratospheric aerosols, and the forcing due to both surface albedo effect and solar activity. The forcing by stratospheric aerosols is mainly caused by volcanic eruptions. Although these effects can have large impacts on the balance (e.g. up to –3 ± 0.6 W/m^2 due of the eruption of the Mt. Pinatubo in 1991), the lack of a reliable record of episodic volcanic events, especially before the 1960s, makes it hard to project future effects.

Land-use changes can cause changes in the land surface albedo as well. However, the responses differ very much per latitudinal band and per landcover type (the albedo of a cultivated field is affected more by a given snowfall than the albedo of an evergreen forest). Future quantification of this effect is not given in IMAGE 2.2, although IMAGE 2.2 provides an extensive amount of data for future land cover.

Total solar irradiance (TSI) is another factor with many uncertainties. The most important uncertainties, posed in IPCC (2001), are:
- what is the absolute value of the TSI? (only records of the last two decades are available; with many disagreements);
- from what other proxy measure of solar output can the historical variation be deduced? (sunspot numbers, solar diameter etceteras);
- how much impact do variations in stratospheric composition and thermal structure resulting from ultraviolet irradiance have on tropospheric climate? (increase in downward infrared flux by heating the stratosphere; effects of changing ozone concentrations due to changing irradiance);
- how important is the correlation between total cloud cover and cosmic ray fluxes? (are galactic cosmic rays less able to reach the Earth when the sun is more active because of fluctuations in the sun's magnetic field?).

Because of the extent of the uncertainties in the above-mentioned cases, IMAGE 2.2 does not take these possible effects into account. Taking the change in global and annual mean

radiative forcing from 1750 allows IPCC (2001) to give the following estimates for possible mechanisms not taken into account by IMAGE 2.2:

Direct mineral dust aerosols: -0.60 to +0.40 W/m^2;
Aviation-induced cirrus: 0 to +0.04 W/m^2;
Aviation-induced contrails: +0.02 W/m^2;
Land use (albedo): -0.20 W/m^2;
Solar: +0.30 W/m^2.

Note that the choice of the year 1750 is crucial for the estimate of the solar effect. A choice of 1700 would give values about twice as large. Given these values and the different uncertainties, it would seem justified to disregard these effects in IMAGE 2.2 until more is known.

4.2 Calibration

The global and annual mean radiative forcing from 1765 to the early 1990s is projected in Figure 4.1 (the results for 1995 are used for IMAGE 2.2). This figure shows that IMAGE 2.2 returns results for its historical period (1765-1995) that are well in line with the latest scientific information available (IPCC, 2001). The slightly higher value of IMAGE 2.2 for the direct sulphate aerosol forcing (less negative) is the main result of a starting point of -0.3 W/m^2 (Harvey et al., 1997), but is also caused by the decrease in sulphur emissions in China, based on emission data up to 1995.

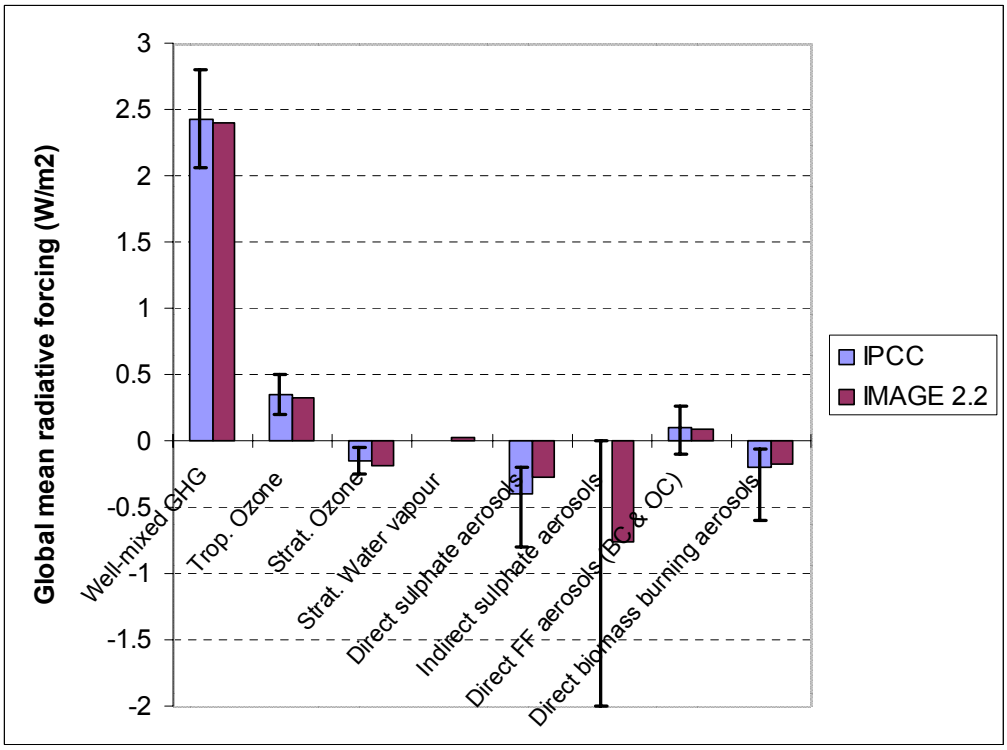

Figure 4.1: Global and annual mean radiative forcing from 1750 to present according IPCC (2001) and from 1765 to 1995 according IMAGE 2.2 (IMAGE team, 2001a). Only the effects taken into account by IMAGE 2.2 are visualised.

The projected changes in radiative forcing are used as input for the Upwelling-Diffusion Climate model (UDCM) of IMAGE 2.2.

4.3 IPCC SRES projections

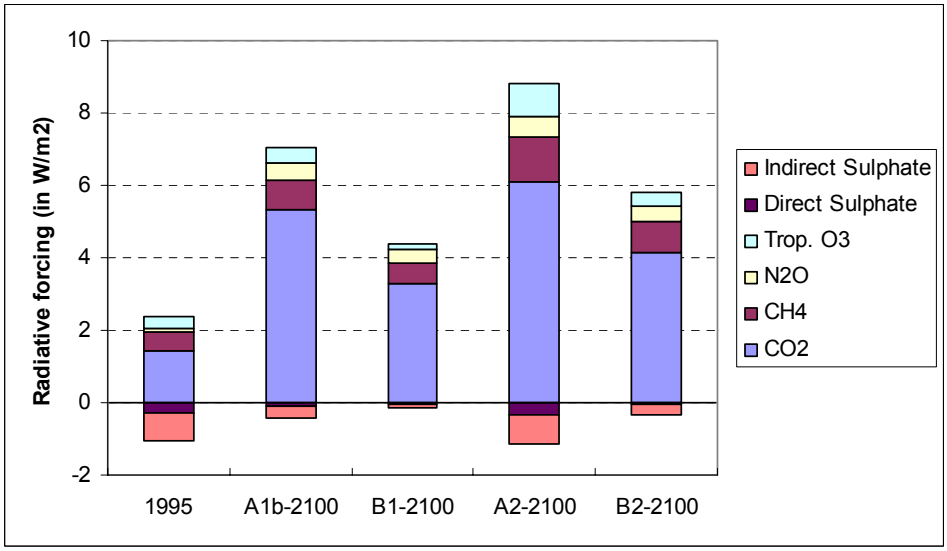

Figure 4.2: Radiative forcing since 1765 for the SRES scenarios according IMAGE 2.2 (IMAGE team, 2001a) for CO_2, CH_4, N_2O, tropospheric O_3 and direct and indirect sulphate aerosols. The values for 1995 are depicted as well.

Figure 4.2 shows the radiative projections for 2100 for the four different SRES scenarios. Clearly, the sustainable scenario B1 has low sulphate forcings because of policies against SO_2 emissions. The differences in the greenhouse gas concentrations, shown in Chapter 3, have their effect on the radiative forcing, as shown in Figure 4.2.

5. Modelling the global-mean temperature change

In IMAGE 2.2 the reaction of the climate system to increased forcing is calculated by a global-mean, upwelling-diffusion, energy-balance model. Section 5.1 describes the methodology of the model. Again, in the following two sections, much attention is paid to calibration of the model and the implementation of the SRES scenarios.

5.1 Methodology

In this section, the methodology of the upwelling-diffusion climate model (UDCM; see Figure 2.1) is explained in further detail. The reader is also referred to Appendix A for further mathematical details. The energy-balance model was introduced in 1985 by Wigley and Schlesinger (1985), and Harvey and Schneider (1985). The elaboration on this model and the inclusion of upwelling-diffusion characteristics was introduced by Wigley and Raper (1987) as the MAGICC model. The latest version of MAGICC (Version 2.4) described here is implemented in IMAGE 2.2. MAGICC is also described in its most recent form in Raper et al. (1996) and Hulme et al. (2000).

The energy-balance model

The model consists of an atmosphere box, coupled to northern and southern hemisphere land and ocean boxes (see Figure 5.1). The two ocean boxes are each divided into 40 layers, with a mixed layer on top that absorbs the energy of solar radiation. Above land, no energy is assumed to be adsorbed. The energy balance of the climate system can be described as:

$$\Delta Q = \lambda \Delta T_a + \Delta F \qquad (5.1)$$

where ΔQ is the global increase in radiative forcing (in $W \cdot m^{-2}$; see Chapter 4) and ΔF the net heat flux into the ocean (in $W \cdot m^{-2}$; both averaged over the entire world area). The term $\lambda \Delta T_a$ is the change in the rate of heat loss to space from the climate system. The feedback parameter, λ, is the inverse of the climate sensitivity (in $°C^{-1}$): the long-term (equilibrium) annual and global-mean surface-air temperature increase for a doubling of the CO_2 concentration since pre-industrial times is denoted by $\Delta T_{2\times}$ (IPCC, 1996). This value is a very important factor for determining the reaction of the climate system (in terms of temperature change) as a response to changes in the CO_2 concentration. In section 5.2, we elaborate further on the uncertainties in the climate sensitivity and its consequences for climate impacts.

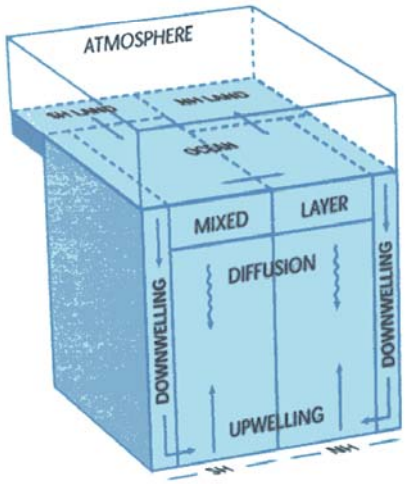

Figure 5.1 The boxes distinguished in the Upwelling-Diffusion Climate Model (Harvey et al., 1997).

Hence, the radiative forcing is partitioned between increased heat loss to space and additional uptake of heat by the climate system (Raper et al., 2001). The absorbed heat is exchanged between the four boxes (determined by k_{LO} and k_{NS}; the land–ocean and northern–southern hemisphere exchange coefficient, respectively). On time scales relevant to climate change, the changes in the atmosphere may be assumed to be in equilibrium with the underlying oceanic mixed layer:

$$C_m \frac{d\Delta T_{O,1}}{dt} = \Delta Q - \lambda \Delta T_a - \Delta F \tag{5.2}$$

where $d\Delta T_{O,1}$ is the temperature change of the oceanic mixed layer and C_m the effective bulk heat capacity of the oceanic mixed layer (Wigley and Schlesinger, 1985).

The four complete equations (including the exchange coefficients land–ocean and the two hemispheres) can be derived from Equation 5.2. The effective bulk heat capacity is expressed as a product of the density of seawater (ρ), the specific heat capacity of water (c) and the height of the oceanic mixed layer (h_m). The four equations are:

$$f_{NO}\left(\rho \cdot c \cdot h_m \frac{d\Delta T_{NO,1}}{dt} - \Delta Q_{NO} + \lambda_O \Delta T_{NO,1} + \Delta F_{NO}\right) = k_{LO}\left(\Delta T_{NL} - \Delta T_{NO,1}\right) + k_{NS}\left(\Delta T_{SO,1} - \Delta T_{NO,1}\right) \tag{5.3}$$

$$f_{SO}\left(\rho \cdot c \cdot h_m \frac{d\Delta T_{SO,1}}{dt} - \Delta Q_{SO} + \lambda_O \Delta T_{SO,1} + \Delta F_{SO}\right) = k_{LO}\left(\Delta T_{SL} - \Delta T_{SO,1}\right) + k_{NS}\left(\Delta T_{NO,1} - \Delta T_{SO,1}\right) \tag{5.4}$$

$$f_{NL}\left(C_l \frac{d\Delta T_{NL}}{dt} - \Delta Q_{NL} + \lambda_L \Delta T_{NL}\right) = k_{LO}\left(\Delta T_{NO,1} - \Delta T_{NL}\right) \tag{5.5}$$

$$f_{SL}\left(C_l \frac{d\Delta T_{SL}}{dt} - \Delta Q_{SL} + \lambda_L \Delta T_{SL}\right) = k_{LO}\left(\Delta T_{SO,1} - \Delta T_{SL}\right) \tag{5.6}$$

where:
f_{NO} = 0.58 (fraction of ocean in the northern hemisphere);
f_{SO} = 0.79 (fraction of ocean in the southern hemisphere);
f_{NL} = 0.42 (fraction of land in the northern hemisphere);
f_{SL} = 0.21 (fraction of land in the southern hemisphere);
ρ = 1.026 x 10^6 g/m^3;
c = 0.9333 cal/g/˚C (one calorie equals 4.1856 Joules);
h_m = 90 m;
C_m = 3.61 x 10^8 J/m^2/˚C (effective bulk heat capacity of mixed layer, calculated by $\rho \cdot c \cdot h_m$, which equals 11.43 W*year/m^2/˚C) ;
C_l = 0.0 W*year/m^2/˚C (effective heat capacity of land surface);
λ_O = feedback parameter above ocean (W/m^2/˚C);
λ_L = feedback parameter above land (W/m^2/˚C);
$\Delta T_{NO,1}$ = temperature change of mixed layer in the northern hemisphere (˚C);
$\Delta T_{SO,1}$ = temperature change of mixed layer in the southern hemisphere (˚C);
ΔT_{NL} = temperature change of land surface in the northern hemisphere (˚C);
ΔT_{SL} = temperature change of land surface in the southern hemisphere (˚C);
k_{LO} = 1.0 W/m^2/˚C (land-ocean exchange coefficient);
k_{NS} = 1.0 W/m^2/˚C (northern-southern hemisphere exchange coefficient).

For the well-mixed gases, the radiative forcings (ΔQ_{XX}) in the four boxes are equal. These radiative forcings are divided to take the non-linear effects of sulfate aerosol into account. Since the approach of Schlesinger et al. (2000) is used in IMAGE 2.2, this division in forcings is not necessary (see Chapter 6). Furthermore, the difference in feedback parameters above the land and ocean is explained in Appendix A.

As stated, the land surface layer does not absorb any energy (C_l = 0.0). Hence, equation 5.5[9] evolves as follows:

$$\frac{k_{LO}}{f_{NL}}\left(\Delta T_{NL} - \Delta T_{NO,1}\right) = \Delta Q_{NL} - \lambda_L \Delta T_{NL} \tag{5.7}$$

Substitute equation 5.7 into 5.3:

$$f_{NO}\left(\rho \cdot c \cdot h_m \frac{d\Delta T_{NO,1}}{dt} - \Delta Q_{NO} + \lambda_O \Delta T_{NO,1} + \Delta F_{NO}\right) = f_{NL}\Delta Q_{NL} - f_{NL}\lambda_{NL}\Delta T_{NL} + k_{NS}\left(\Delta T_{SO,1} - \Delta T_{NO,1}\right) \tag{5.8}$$

$\frac{d\Delta T_{NO,1}}{dt}$ can be calculated from equation 5.8. For this purpose, the heat flux into the ocean (ΔF_{NO}) needs to be calculated first. This heat flux is dependent on the 40 ocean layers, with important parameters being the upwelling rate (w) and the diffusivity (K). Below, we elaborate on the oceanic upwelling-diffusive part of the model.

[9] The methodology is only explained for the Northern Hemisphere. Logically, the methodology is exactly the same for the Southern Hemisphere.

The upwelling-diffusive model
The ocean is considered one-dimensional, with 40 layers in each hemisphere. The temperature of the mixed layer ($T_{NO,1}$) is constant, with 17.2˚C as initial value. The bottom layer of the ocean ($T_{NO,40}$) has an initial value of 1.0˚C. The temperature profile is described according the following equation:

$$T_{NO,x} = T_{NO,40} + \left(T_{NO,1} - T_{NO,40}\right) \cdot \exp\left(-\frac{w_0 \cdot z(x)}{K}\right) \quad (5.9)$$

with:
x = 2,…,40 (number of ocean layers under the mixed layer);
w_0 = 4.0 m/yr (initial upwelling rate);
$z(x)$ = 50,…,3850 m (distance from the bottom of mixed layer to the middle of each layer);
K = 1.0 cm^2/sec = 3155.76 m^2/yr (vertical diffusivity).

The initial temperature profile is depicted in Figure 5.2. The vertical mixing processes in the ocean are represented by vertical diffusivity and upwelling, assumed to be vertically uniform. Hence, the temperature change in the ocean can be estimated according the following description:

$$\frac{\partial \Delta T_{NO,x}}{\partial t} = K \frac{\partial^2 \Delta T_{NO,x}}{\partial z^2} + w \frac{\partial \Delta T_{NO,x}}{\partial z} \quad (5.10)$$

where K symbolises the diffusivity (in m^2 per year), w the upwelling rate (in m per year), z the depth of the ocean in which the process occurs (in m) and t the timestep (in years). The height of the mixed layer (h_m) is assumed to be 90 metres and the height of the other layers (d) is assumed to be 100 metres.

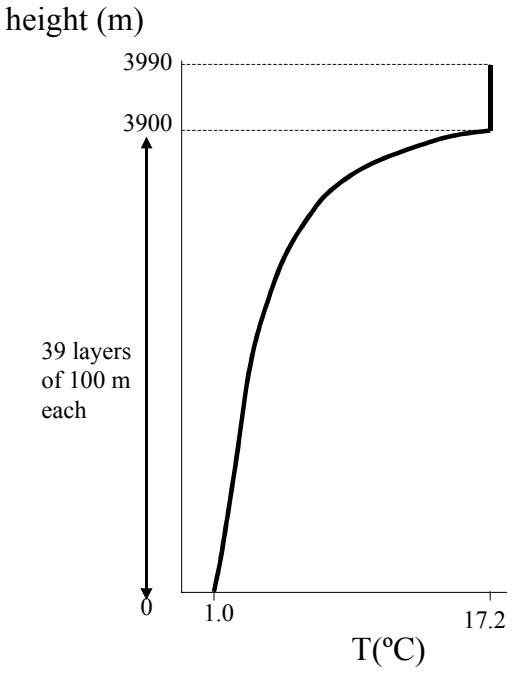

Figure 5.2 The initial temperature profile of the ocean. The temperature in the oceanic mixed layer is considered to be constant.

The diffusivity and upwelling processes occur between each ocean layer. To implement the thermohaline circulation in this one-dimensional model, a downwelling process is added from the mixed layer to the bottom layer in the Polar Regions. This process is regulated by the factor π; the temperature change ratio from polar to non-polar regions. Different GCM simulations show a reduction in upwelling rate as greenhouse-gas-induced warming increases. This mechanism is handled by applying a relationship between w and the ocean surface-temperature change, given by:

$$w(t) = w_0\left(1 - \frac{\Delta T}{\Delta T^+}\right) \tag{5.11}$$

where ΔT^+ is a tunable parameter representing the magnitude of warming that would result in zero upwelling (Raper et al., 1996). A collapse of the thermohaline circulation would result in a deeper penetration of warm water in the deep ocean. However, a zero upwelling is not likely to occur, not even when the thermohaline circulation has stopped, because of meridional overturning stream functions of the ocean (see Figure 5.3). These functions show a number of isolines in the ocean, returning a flow from high ocean layers in the high latitude regions to oceanic bottom layers in the mid-latitude regions. These flows will preserve the existing upwelling in the ocean (Raper et al., 2001). Therefore, equation 5.11 is only applied to 30% of the upwelling. The other 70% is assumed to be constant, which better fits GCM simulations (Raper et al., 2001).

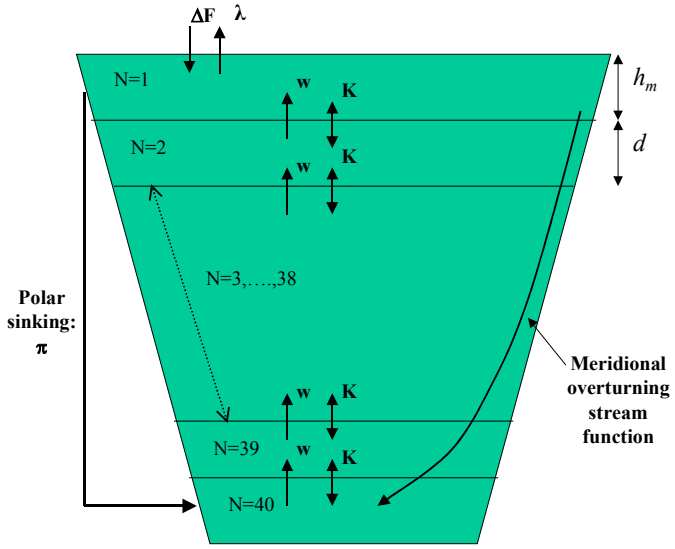

Figure 5.3 Schematic view of the ocean and its main fluxes.

Consequently, the function of ΔF_{NO} can be formulated as:

$$\Delta F_{NO} = \frac{\rho \cdot c \cdot K\left(\Delta T_{NO,1} - \Delta T_{NO,2}\right)}{0.5d} - \rho \cdot c \cdot w\left(\Delta T_{NO,2} - \pi \cdot \Delta T_{NO,1}\right) \tag{5.12}$$

with:
$\Delta T_{NO,2}$ = temperature change of the first layer beneath the mixed layer;
d = 100 m (height of the other 39 ocean layers).

The factor 0.5 relates to the application of the diffusion and upwelling process to the middle of each layer.

Equation 5.12 can be implemented in Equation 5.8. Moreover, rewriting Equation 5.5 brings back the following calculation of the change in land temperature in the Northern Hemisphere:

$$\Delta T_{NL} = \frac{f_{NL}\Delta Q_{NL}}{f_{NL}\cdot\lambda_L + k_{LO}} + \frac{k_{LO}\Delta T_{NO,1}}{f_{NL}\cdot\lambda_L + k_{LO}} \qquad (5.13)$$

Implementing Equation 5.13 in Equation 5.8 brings back a complex calculating scheme for solving the temperature change of the oceanic mixed layer. And Equation 5.13 can be solved as well with a calculated $\Delta T_{NO,1}$. The calculation of the temperature change in the oceanic layers is further worked out in Appendix B.

When the temperature changes of all the oceanic layers are calculated, the temperature change above the land (ΔT_{NL}) can be calculated as well (Equation 5.13). The same approach for the Southern Hemisphere brings back a change in temperature for the four upper layers of the four boxes mentioned in the Equations 5.3, 5.4, 5.5 and 5.6 (see also Figure 5.1). The global-mean temperature change of the total surface layer is returned by the mean of these four temperature changes. For further information on the MAGICC model, the reader is referred to Wigley and Raper (1987, 1992, 1993, 1995), Raper et al. (1996) and Hulme et al. (2000).

5.2 Calibration

The large heat capacity of the oceans plays an important role in the time-dependent response of the climate system to external forcing. Transport of heat to the deep ocean layers effectively slows down the surface-air temperature response over ocean and land surfaces, as well as in the atmosphere. If the time horizon of a climate change analysis only extends over a few years or decades, response is dominated by the upper ocean surface layer, reaching relatively rapid adjustment within a few decades. Still, a significant part, roughly 50 %, of the final global warming will manifest itself decades to centuries later. The delay caused by penetration of heat to the deeper ocean layers is also what causes sea-level rise to continue long after stabilisation of greenhouse gas concentrations (Wigley and Raper, 1993). The balance between the rapid and slow adjustment terms is a source of uncertainty, as it depends on non-linear processes like stratification of the upper ocean layers.

Climate sensitivity (λ^{-1}; see section 5.1) is another important source of uncertainty in climate response to external forcing. Here, the IPCC (1996) definition is used: the long-term (equilibrium) annual and global-mean surface-air temperature increase for a doubling CO_2 concentration, denoted by $\Delta T_{2\times}$. Climate sensitivity is an outcome of all geophysical feedback mechanisms and their associated uncertainties. The most important source of uncertainty is the hydrological cycle, in particular, clouds and their interaction with radiative processes. IPCC (1996) has estimated the climate sensitivity to lie within the range of 1.5 to 4.5°C, with a 'best-guess' value of 2.5°C. This 'best-guess' has been used as default setting throughout the IMAGE 2.2 model.

To test the uncertainty related to the climate sensitivity, IMAGE 2.2 is also used with respective low (1.5°C) and high (4.5°C) climate sensitivities. Runs with changed climate sensitivity are provided for the A1F (A1F low, A1F high) and B1 (B1 low, B1 high)

scenarios on the main disc (IMAGE team, 2001a). These scenarios span the full range of the SRES emission scenarios and therefore adequately illustrate the uncertainty of different climate sensitivities. This full range of the global-mean surface temperature is depicted in Figure 3.4. Note that the IPCC range of the projections for the global average temperature change since 1990 is stated as 1.4 to 5.8°C (IPCC, 2001). The IMAGE 2.2 results are very similar to this range when the uncertainty in the climate sensitivity is taken into account (compared to 1990 the IMAGE 2.2 range is from 1.3 to 5.0°C; see Figure 3.4). Since pre-industrial age the global-mean surface temperature change for 2000 has occurred between 0.4°C (low sensitivity) and 0.8°C (high sensitivity), with a median of 0.6°C for the 'best-guess' value of the climate sensitivity (see Figure 3.4). These IMAGE 2.2 results are well within the range of the observed increase over the 20th century (since 1861), as reported in IPCC (2001): 0.6 ± 0.2°C.

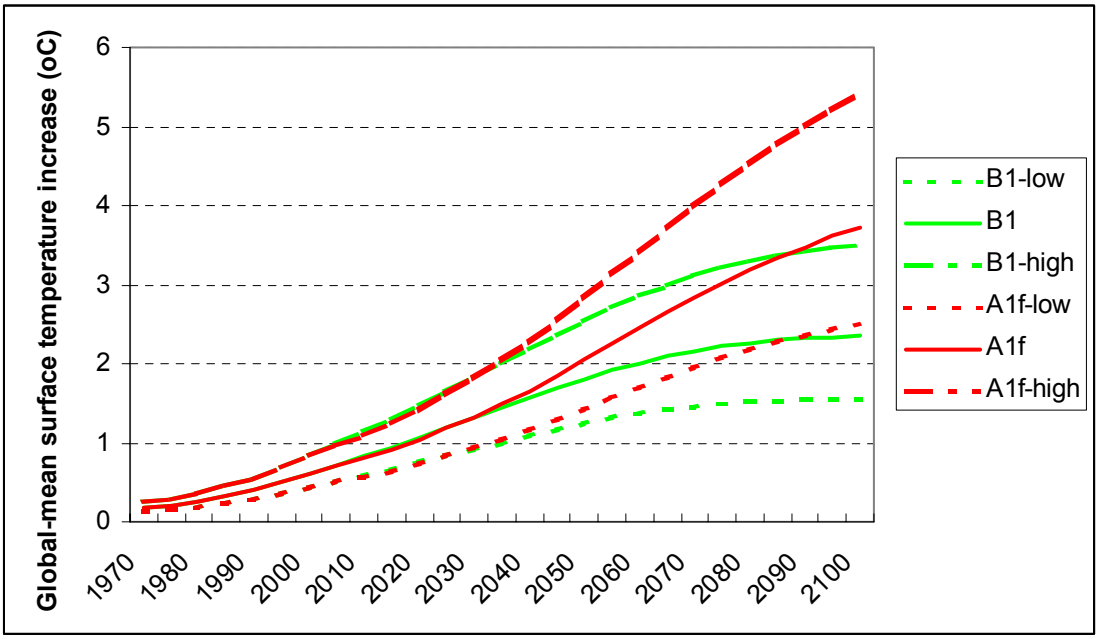

Figure 5.4: Global-mean surface temperature change since the pre-industrial age for the B1 and A1f scenario with different climate sensitivities (IMAGE team, 2001a). High denotes a climate sensitivity of 4.5°C and low a climate sensitivity of 1.5°C. The default setting of the climate sensitivity in IMAGE 2.2 is 2.5°C.

5.3 IPCC SRES projections

The IMAGE 2.2 results for the four SRES scenarios are depicted in Figure 5.5. The high economic growth scenario A1b has the fastest increasing temperature in the first half of the 21st century. In the second half of the 21st century, the population declines and the high technological development requires less agricultural land to fulfill the food demand. Whereas the CO_2 concentration of the A2 scenario intersects with the A1b scenario around 2075 (see Figure 3.4), the temperature profile does not intersect until 2090. This shows the time delays in the climate system, as discussed in this chapter.

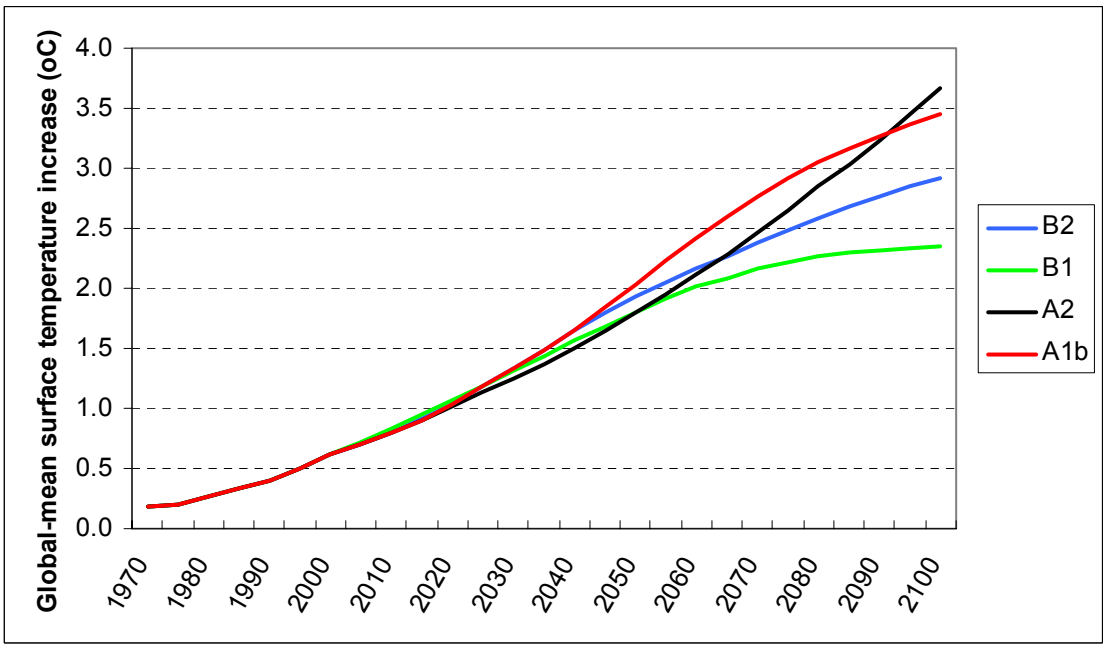

Figure 5.5: Global-mean surface temperature change since 1765 for the SRES scenarios (IPCC, 2000) as implemented by the IMAGE 2.2 model (IMAGE team, 2001a).

6. Impacts of temperature change

As mentioned in Chapter 3, the calculated global-mean temperature change decreases the oceanic carbon uptake of the ocean (see Equation 3.5). However, the change in global-mean temperature has an effect on many other aspects of the biosphere-atmosphere-ocean system. In this chapter the impact on sea-level rise is further explained in section 6.1. And finally, the pattern-scaling of the global-mean temperature to grid-specific temperature and precipitation changes is explained briefly in section 6.2. This pattern-scaling is required by the TES of IMAGE 2.2 for the grid-specific climate conditions that determine potential vegetation and potential yields.

6.1 Sea-level rise model (SLRM)

The impacts of global warming on global sea level are calculated by the Sea-Level Rise Model of IMAGE 2.2 (SLRM) and correspond with the sea-level rise model of the MAGICC model described in Raper *et al.* (1996). In this model the total sea-level rise is influenced by thermal expansion of the oceans and by changing the net mass balance of glaciers and ice sheets. The most important ice sheets of Greenland and Antarctica are taken into account in SLRM.

Thermal expansion

As the ocean warms, the density of the ocean decreases and its volume increases. The temperature changes in each ocean layer, calculated in UDCM (see Chapter 3), are used to determine the expansion coefficient. The initial vertical temperature profile is based on observations from Levitus (1982). The initial temperature of the oceanic mixed upper layer is assumed to be 17.2°C, while the temperature of deeper ocean layers is assumed to decrease in depth to a temperature of 1.0°C for the bottom layer.

Influence of small glaciers

Melting of small glaciers may also contribute to sea-level rise. A simple approach to relate glacier volume to temperature change is used for the small glaciers, as described in detail by Wigley and Raper (1995). The three important parameters in this approach are:

- the initial (1880) global ice volume;
- the minimum temperature increase that would cause a given glacier to disappear, and
- the glacier-response time.

A distribution of values for the minimum temperature and glacier response time is assumed to take different glaciers into account. The glacier-response time varies from 70 to 130 years and the minimum temperature from 0.7°C to 3.0°C. The initial global ice volume is assumed to be a 30-cm sea-level equivalent.

Influence of Antarctica and Greenland

For Greenland and Antarctica, the ice sheet area is assumed to be constant, because the response times are very long and temperature changes are assumed to be moderate. The mass balance of the ice sheets can be divided into two components:

- a constant component representing the gain or loss of ice as a result of the initial state of the ice sheet;
- a component that is linearly dependent on the temperature change relative to the initial state. Just as for small glaciers, the initial state of the ice sheets is assumed to be the year 1880.

The Greenland ice sheet is assumed to be in equilibrium in 1880, so that the constant component is 0.0 cm per year. For Antarctica this component is assumed to be 0.01 cm per year. The sensitivity values for the mass balance are taken as 0.03 cm per year per °C for Greenland and 0.02 cm per year per °C for Antarctica. The sensitivity values are based on estimates of the sensitivity of the ice sheets to 1°C warming as computed by more complex two- and three-dimensional ice sheet models (Wigley and Raper, 1995).

The West Antarctic Ice Sheet (WAIS) contains enough ice to raise the sea level by 6 metres; it has attracted extra attention because it may result in rapid ice discharge due to weak surrounding ice shelves. However, this was concluded as being very unlikely to happen in the 21st century (IPCC, 2001).

Uncertainties
The uncertainty in these indicators is large, with ranges for 1990-2100 of 0.11 to 0.43 m for thermal expansion, 0.04 to 0.17 m for the glacier contribution, -0.01 to 0.07 m for the Greenland ice sheet and -0.12 to -0.02 m for the Antarctica contribution.

IPCC SRES projections
In Figure 6.1 we plotted the total sea-level rise for the SRES scenarios. Again, a time-delay is visible if we compare the CO_2 concentration profiles (Figure 3.4), the global-mean surface temperature (Figure 5.5) and this sea-level rise. The differences between the scenarios are very small and the A1b scenario returns the highest sea-level rise. This means that even hundreds of years after 2100 sea level will rise because of greenhouse gas emissions and the associated greenhouse gas concentrations.

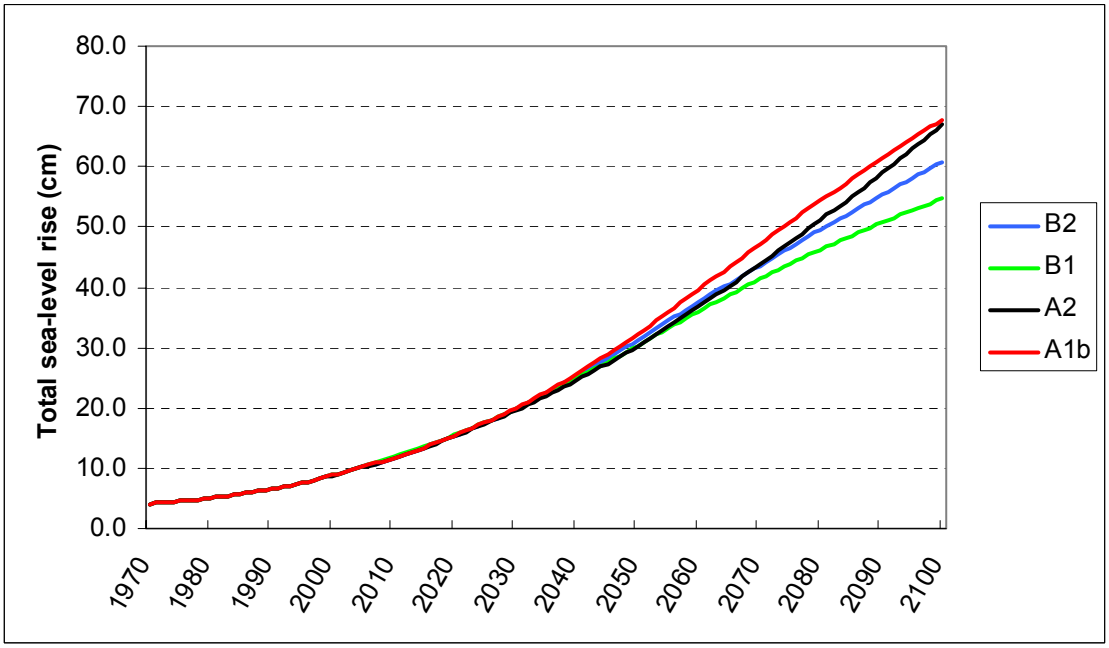

Figure 6.1: Total sea-level rise since 1765 for the SRES scenarios (IPCC, 2000) as implemented by the IMAGE 2.2 model (IMAGE team, 2001a).

6.2 Geographical Pattern Scaling (GPS)

The condition is that a GCM with a climate-change pattern due only to changes in greenhouse gases is used for the pattern scaling. If a GCM climate-change pattern is obtained by increased greenhouse gases and aerosols, the radiative forcings differ per hemisphere, and per land or ocean. The division of the radiative forcings of aerosols over the four boxes is calculated with the following ratios (Wigley and Raper, 1992 and Raper et al., 1996):

- 4:1 for the direct forcing between northern and southern hemisphere;
- 2:1 for the indirect forcing between Northern and Southern Hemisphere;
- 99:1 for the ozone forcing between the Northern and Southern Hemisphere;
- 9:1 within each hemisphere between land and ocean for all of the three groups, mentioned above.

The climate-change patterns are not simulated explicitly in IMAGE 2.2. The global-mean surface temperature change, output of UDCM, needs to be linked to a monthly 0.5 x 0.5 degree grid, considering the requirements of the Terrestrial Environment System of IMAGE 2.2. This linking is applied by using the standardised IPCC pattern-scaling approach (Carter et al., 1994).

In this approach, the General Circulation Model (GCM) results of a control equilibrium climate are subtracted from the GCM results of an equilibrium experiment climate (i.e., doubled CO_2). This gives (monthly) geographical distributions of experiment-induced equilibrium climate change ($\Delta Q_{GCM,cell(m)}$). The normalization of these GCM results is done by the corresponding change in annual global-men surface temperature ($\Delta \overline{T}_{GCM,global} = \overline{T}_{GCM-\exp,global} - \overline{T}_{GCM-con,global}$). Next, the global-mean surface temperature change from UDCM is used as multiplicator to obtain the time-dependent geographical distributions of climate change (per month) relative to the reference year (1990). Thus, the global-mean surface temperature from UDCM is also relative to 1990. In equation:

$$Q_{cell(m)}(t) = \frac{\Delta Q_{GCM,cell(m)}}{\Delta \overline{T}_{GCM,global}} \cdot \Delta \overline{T}_{UDCM,global}(t) \qquad (6.1)$$

the monthly, observed climate data are added to obtain the absolute values. In IMAGE 2.2, uses the observed data of the 1961-90 mean climate (New et al., 1999). This well-known approach is already implemented in IMAGE 2.1 (Alcamo et al., 1998).

This simple, computationally practicable approach is necessary because many uncertainties exist on the future emissions of greenhouse gases and SO_2 and hence, it would be computationally impossible to perform numerous emission scenarios with a GCM to span the full range of possibilities. Furthermore, the sensitivity of the climate system and the forcing by the sulfate aerosols are highly uncertain. To assess the consequences of different climate sensitivities, UDCM can be used with different settings (see Chapter 5). To take the uncertainties in the forcing by sulfate aerosols into account, IMAGE 2.2 uses results from the AGC/MLO model (11-layer troposphere/lower-stratosphere general circulation/mixed-layer-ocean) from the University of Illinois at Urbana-Champaign (UIUC). The approach, introduced by Schlesinger et al. (2000), takes the non-linear effects of sulfate aerosols into account. It consists of the following 8 steps:

1. A first run based on the climate forcing after 1990 by greenhouse gases only. The corresponding climate change is scaled with a greenhouse gas-only pattern from a selected GCM (see Equation 6.1). The Hadley GCM run with greenhouse gases only (HADCM2) is used as default in IMAGE 2.2.
2. A second run using climate forcing by sulfate only (other greenhouse gases held constant after 1990). Forcing is calculated as described in section 4.1, Equations 4.6 and 4.7. Only the corresponding temperature change is scaled with a sulfate-only pattern from the AGC/MLO model. The sulfate-only pattern is constructed using a $10xSO_4$ simulation by AGC/MLO. A $1xSO_4$ simulation is not used because the corresponding forcing (-0.55 W/m^2) yields a change in the global-mean surface temperature that is not much larger than the year-to-year variability of the control simulation (Schlesinger et al., 2000). Schlesinger et al. (2000) show that it is justifiable to use the same climate sensitivity in UDCM for this run as for the greenhouse gases-only run. The results of the first and second runs are added (no weights given) to obtain the combined pattern of radiative forcings by greenhouse gases and sulfate aerosols.

3-8. So far, only linear responses are taken into account. Runs 3-8 are made to account for the non-linear climate response to radiative forcing by sulfate aerosols. These steps are only applied to the temperature change patterns of GCMs. There is too little known about cloud formation to apply this method to precipitation patterns.

The assumption in this approach is that the response to sulfate forcing is almost linear. Hence, the sum of runs 1 and 2 comes close to representing the climate changes correctly. However, because of local climate circumstances, it matters globally whether SO_2 emissions increase in, for example, China or in the USA. Thus, the increase of SO_2 emissions in different world regions since 1990 are translated into global-mean changes in radiative forcing and are scaled with a specific climate change pattern. This specific climate change pattern is obtained by an experiment run with $10xSO_4$ forcing in those world regions. These climate change patterns originate in the AGC/MLO model. The AGC/MLO model has delivered sulfate-only results for six world regions. In Table 6.1, these six regions are compared with the IMAGE 2.2 regions that coincide with these regions (see Figure 1.2 for the IMAGE 2.2 regions). The weights of the six regional patterns are calculated as follows (Schlesinger et al., 2000):

- First, the regional sulfate burden in 1990 is calculated using regression equations presented by Schlesinger et al. (2000), relating the sulfate aerosol burden (mg/m^2) and annual SO_2 emissions (g/m^2) for the six regions (i);
- The ratio g_i of the sulfate burden in region i to the global sulfate aerosol burden is calculated for the year 1990 (no scenario dependency);
- The future ratios of regional to global sulfate burden are calculated for each scenario using the same regression equations. This gives time-dependent ratios $f_{i,j}$;
- The weight factor $d_{i,j}$ is calculated as follows: $d_{i,j} = g_i - f_{i,j}$;
- For the years after 1990, the weight factor $d_{i,j}$ is used to multiply the regional forcings, calculated from the emissions of SO_2 in (see Equations 4.6 and 4.7);
- The temperature changes from runs 3-8 are scaled with the six AGC/MLO patterns, constructed with increased forcings in the six UIUC regions;
- These six scaled temperature patterns are added to the combined pattern of the first two runs for forcing by greenhouse gases only and sulfate only. In this way, the combination of the first two runs is corrected for the regional differences in forcing by future SO_2 emissions (see Equation 6.1; with i as index for the six UIUC regions).

$$\Delta T_{cell(m)}(t) = \frac{\Delta T_{GCM-GHGonly,cell(m)}}{\Delta \overline{T}_{GCM-GHGonly,global}} \cdot \Delta \overline{T}_{UDCM-GHGonly,global}(t) + \frac{\Delta T_{AGC/MLO-SO_4only,cell(m)}}{\Delta \overline{T}_{AGC/MLO-SO_4only,global}} \cdot \Delta \overline{T}_{UDCM-SO_4only,global}(t) + \sum_{i=1}^{6} \frac{\Delta T_{i,AGC/MLO-SO_4only,cell(m)}}{\Delta \overline{T}_{i,AGC/MLO-SO_4only,global}} \cdot \Delta \overline{T}_{i,UDCM-SO_4only,global}(t) \quad (6.2)$$

Table 6.1: The 6 world regions from UIUC (Schlesinger et al., 2000) compared with the 17 IMAGE 2.2 world regions (IMAGE team, 2001a)

UIUC regions	*IMAGE 2.2 regions*
North America	• Canada • USA • Central America
North Africa	• Northern Africa • Western Africa • Eastern Africa • Middle East • South Asia
Europe	• OECD Europe • Eastern Europe
Siberia	• Former USSR
Asia	• East Asia • South East Asia • Japan
Southern Hemisphere	• South America • Southern Africa • Oceania

References

Alcamo, J., G.J.J. Kreileman, M.S. Krol, R. Leemans, J.C. Bollen, J.G. van Minnen, M. Schaeffer, A.M.C. Toet and H.J.M. de Vries, 1998. Global modelling of environmental change: on overview of IMAGE 2.1. In: J. Alcamo, R. Leemans and G.J.J. Kreileman (Eds.), Global change scenarios of the 21st century. Results from the IMAGE 2.1 model. Elsevier Science, London, United Kingdom, pp. 3-94.

Alfsen, K.H. and T. Berntsen, 1999. An efficient and accurate carbon cycle model for use in simple climate models. CICERO Working Paper 1999:1. Center for International Climate and Environmental Research, Oslo, Norway, 14 pp.

Carter, T.R., M.L. Parry, H. Harasawa and S. Nishioka, 1994. IPCC Technical Guidelines for Assessing Climate Change Impacts and Adaptations. IPCC Special Report 0904813118. Intergovernmental Panel on Climate Change, WMO and UNEP, Geneva.

CPB. 1999. WorldScan: the core version. The Hague: CPB Netherlands Bureau for Economic Policy Analysis. pp 137.

De Haan, B. J., M. Jonas, O. Klepper, J. Krabek, M.S. Krol and K. Olendrzynki, 1994. An atmosphere-ocean model for integrated assessing of global change. Water, Air and Soil Pollution, 76: 283-318.

Den Elzen, M.G.J., 1998. The meta-IMAGE 2.1 model: an interactive tool to assess global climate change. RIVM-report no. 461502020. National Institute for Public Health and the Environment, Bilthoven, 49 pp.

Den Elzen, M.G.J. and M. Schaeffer, 2002. Assessment of major uncertainties in calculating regional contributions to climate change. RIVM-report no. 728001012. National Institute for Public Health and the Environment, Bilthoven, 41 pp.

De Vries, H.J.M., D.P. van Vuuren, M.G.J. den Elzen and M.A. Janssen, 2001. The TARGETS-IMAGE energy regional model (TIMER): Technical documentation. RIVM-report no. 481508014. National Institute for Public Health and the Environment, Bilthoven.

Eickhout, B., 1999. IMAGE en MOGUNTIA vergeleken. Het belang van de troposferische chemie in klimaatmodellen. Internal report, National Institute for Public Health and the Environment / the University of Nijmegen (in Dutch only).

Harvey, L.D. and S.H. Schneider, 1985. Transient Climate Response to External Forcing on 100-104 Year Time Scales. Part 1: Experiments with Globally Averaged, Coupled, Atmosphere and Ocean Energy Balance models. Journal of Geophysical Research, 90, 2191-2205.

Harvey, D., J. Gregory, M. Hoffert, A. Jain, M. Lal, R. Leemans, S. Raper, T. Wigley and J. de Wolde, 1997. An introduction to simple climate models used in the IPCC second assessment report. IPCC Technical Paper II, Geneva, Switzerland, 47 pp.

Hilderink, H.B.M. 1999. Population in Transition: An integrated regional modeling framework. Ph.D. Thesis. Groningen: University of Groningen.

Houghton, R. A., J. L. Hackler, and K. T. Lawrence. 1999. The US carbon budget: Contributions from land-use change. Science, 285, 574-578.

Hulme, M., T. Wigley, E. Barrow, S. Raper, A. Centella, S. Smith and A. Chipanski, 2000. Using a climate scenario generator for vulnerability and adaptation assessments: MAGICC and SCENGEN version 2.4 workbook. Norwich, UK, 52 pp.

IMAGE team, 2001a. The IMAGE 2.2 implementation of the SRES scenarios. A comprehensive analysis of emissions, climate change and impacts in the 21st century. RIVM CD-ROM publication 481508018, National Institute for Public Health and the Environment, Bilthoven, the Netherlands.

IMAGE team, 2001b. The IMAGE 2.2 implementation of the SRES scenarios: Climate change scenarios resulting from runs with several GCMs. RIVM CD-ROM Publication 481508019, National Institute for Public Health and the Environment, Bilthoven, the Netherlands.

IPCC, 1996. Climate Change 1995: The science of climate change. Contribution of Working Group I to the Second Assessment Report of the Intergovernmental Panel on Climate Change [J.T. Houghton, L.G. Meira Filho, B.A. Callander, N. Harris, A. Kattenberg and K. Maskell (eds.)]. Cambridge University Press, Cambridge, United Kingdom, New York, NY, U.S.A. and Melbourne, Australia, 572 pp.

IPCC, 2000. Special Report on Emissions Scenarios. A Special Report of Working Group III of the Intergovernmental Panel on Climate Change. Cambridge University Press, Cambridge, United Kingdom, New York, NY, U.S.A., Melbourne, Australia and Madrid, Spain, 599 pp.

IPCC, 2001. Climate Change 2001: The scientific basis. Contribution of Working Group I to the Third Assessment Report of the Intergovernmental Panel on Climate Change [J.T. Houghton, Y. Ding, D.J. Griggs, M. Noguer, P.J. van der Linden, X. Dai, K. Maskell and C.A. Johnson (eds.)]. Cambridge University Press, Cambridge, United Kingdom and New York, NY, U.S.A., 881 pp.

Jones, P.D. and T.M.L. Wigley, 1995. Detection of greenhouse-gas-induced climatic change. Progress Report covering the period 1 July 1994 – 31 July 1995. Grant No. DE-FG02-86ER60397-A014. Climatic Research Unit, University of East Anglia, Norwich, U.K.

Joos, F., M. Bruno, R. Fink, U. Siegenthaler, T.F. Stocker, C. Le Quéré and J.L. Sarmiento, 1996. An efficient and accurate representation of complex oceanic and biospheric models of anthropogenic carbon uptake. Tellus, 48B, 397-417.

Joos, F., G.-K. Plattner, T.F. Stocker, O. Marchal and A. Schmittner, 1999. Global warming and marine carbon cycle feedbacks on future atmospheric CO_2. Science, 284, 464-467.

Joos, F., I.C. Prentice, S. Sitch, R. Meyer, G. Hooss, G.-K. Plattner, S. Gerber and K. Hasselmann, 2001. Global warming feedbacks on terrestrial carbon uptake under the Intergovernmental Panel on Climate Change (IPCC) emission scenarios. Global Biogeochemical Cycles, 15:4, 891-907.

Keeling, C. D., and T. P. Whorf. 2001. Atmospheric CO_2 records from sites in the SIO air sampling network. In: Trends: A Compendium of Data on Global Change. Carbon Dioxide Information Analysis Center, Oak Ridge National Laboratory, Oak Ridge.

Krol, M. S. and H. van der Woerd, 1994. Atmospheric composition calculation for evaluation of climate scenarios. Water, Air and Soil Pollution, 76, 259-281.

Leemans, R., B. Eickhout, B. Strengers, L. Bouwman and M. Schaeffer, 2002. The consequences of uncertainties in land use, climate and vegetation responses on the terrestrial carbon. Science in China, Ser.C, 45 (Supp.), 126.

Levitus, S., 1982. Climatological atlas of the world oceans. NOAA Professional paper 13, U.S. Government Printing Office, Washington, D.C., U.S.A.

Marland, G., and T. A. Boden. 2000. Global, Regional, and National CO_2 Emissions. In: Trends: A Compendium of Data on Global Change. Carbon Dioxide Information Analysis Center, Oak Ridge National Laboratory, Oak Ridge.

New, M., M. Hulme and P. Jones, 1999. Representing twentieth-century space-time climate variability. Part I: Development of a 1961-90 mean monthly terrestrial climatology. Journal of Climate, 12: 829-856.

Olivier, J.G.J., A.F. Bouwman, C.W.M. van der Maas, J.J.M. Berdowski, C. Veldt, J.P.J. Bloos, A.J.H. Visschedijk, P.Y.J. Zandveld and J.L. Haverlag, 1996. Description of EDGAR Version 2.0. A set of global emission inventories of greenhouse gases and ozone-depleting substances for all anthropogenic and most natural sources on a per country basis and on 1ox1o grid. RIVM-report no. 771060002/ TNO MEP Report no. R96/119. National Institute for Public Health and the Environment, Bilthoven.

Opsteegh, J. D., R.J. Haarsma, F.M. Selten and A. Kattenberg, 1998. ECBilt: a dynamic alternative to mixed boundary conditions in ocean models. Tellus, 50A, 348-367.

Raper, S.C.B., J.M. Gregory and T.J. Osborn, 2001. Use of an upwelling-diffusion energy balance climate model to simulate and diagnose A/OGCM results. Climate Dynamics, 17, 601-613.

Raper, S.C.B., T.M.L. Wigley and R.A. Warrick, 1996. Global sea-level rise: past and future. In: J.D. Milliman and B.U. Haq (Eds.), Global sea-level rise: past and future. Kluwer Academic Publishers, Dordrecht, The Netherlands, pp. 11-45.

Schlesinger, M.E., S. Malyshev, E.V. Rozanov, F. Yang, N.G. Andronova, H.J.M. de Vries, A. Grübler, K. Jiang, T. Masui, T. Morita, J. Penner, W. Pepper, A. Sankovski and Y. Zhang, 2000. Geographical distributions of temperature change for scenarios of greenhouse gas and sulfur dioxide emissions. Technological Forecasting and Social Change, 65: 167-193.

Strengers, B., 2001. The agricultural economy model in IMAGE 2.2. RIVM-report no. 481508015. National Institute for Public Health and the Environment, Bilthoven, The Netherlands.

Strengers, B., R. Leemans, B. Eickhout, B. de Vries and A.F. Bouwman, 2004. The land use projections in the IPCC SRES scenarios as simulated by the IMAGE 2.2 model. Geojournal, (in press).

Takahashi, T., J. Olafsson, J.G. Goddard, D.W. Chipman and S.C. Sutherland, 1993. Seasonal variation of CO_2 and nutrients in the high-latitude surface oceans: A comparative study. Global Biogeochemical Cycles, 7, 843-878.

The, T.H.P., 1997. Description of a transport chemistry toolbox: a new implementation of MOGUNTIA. RIVM-report no. 722201008. National Institute for Public Health and the Environment, Bilthoven, The Netherlands.

Tinker, B and the members of the Board, 2000. Report of the third session of the IMAGE advisory board. UNEP/DEIA&EW/TR.99-6 and RIVM-report no. 481508014. National Institute for Public Health and the Environment, Bilthoven, The Netherlands, 33 pp.

Van Minnen, J.G., R. Leemans and F. Ihle. 2000. Defining the importance of including transient ecosystem responses to simulate C-cycle dynamics in a global change model. Global Change Biology, 6: 595-612.

Wigley, T.M.L. and S.C.B. Raper, 1987. Thermal expansion of sea water associated with global warming. Nature, 330, 127-131.

Wigley, T.M.L. and S.C.B. Raper, 1992. Implications for climate and sea level of revised IPCC emissions scenarios. Nature, 357, 293-300.

Wigley, T.M.L. and S.C.B. Raper, 1993. Future changes in global mean temperature and sea level. In: R.A. Warrick, Barrow and T.M.L. Wigley (Eds.), Climate and Sea Level Change: Observations, Projections and Implications. Cambridge University Press, Cambridge, United Kingdom, pp. 111-133.

Wigley, T.M.L. and S.C.B. Raper, 1995. An heuristic model for sea level rise due to the melting of small glaciers. Geophysical Research Letters, 22, 2749-2752.

Wigley, T.M.L. and M.E. Schlesinger, 1985. Analytical solution for the effect of increasing CO2 on global mean temperature. Nature, 315, 649-652.

Zimmerman, P.H., 1988. MOGUNTIA: A handy global tracer model. Air pollution modeling and its applications, volume VI. Edited by H. van Dop. NATO/CCMS, Plenum, New York.

Appendix A: Partitioned feedback parameters

As mentioned in Chapter 5, section 5.1.1, a differentiation in the sensitivity coefficient above land and ocean has been made to make the upwelling-diffusion, energy-balance climate model comparable with GCMs (Jones and Wigley, 1995). To obtain λ_{Ocean} and λ_{Land}, a relationship with the globally defined $\Delta T_{2\times}$ has to be defined. For this relationship an external given ratio between land and ocean warming ($R = \Delta T_L/\Delta T_{O,1}$) is assumed. The following derivation is taken from Jones and Wigley (1995).

First, to calculate the different feedback coefficients over the land and ocean, the ocean is assumed to be in a steady state. Hence, the relationship as stated in Equation 5.1 evolves as follows:

$$\Delta Q = \lambda \Delta T_a = \lambda\left(f_O \Delta T_{O,1} + f_L \Delta T_L\right) \quad \text{(A.1)}$$

Consequently, the equations for the four boxes as depicted in Figure 5.1 can be described as follows:

$$f_{NO}\lambda_O \Delta T_{NO,1} = f_{NO}\Delta Q_{NO} + k_{LO}\left(\Delta T_{NL} - \Delta T_{NO,1}\right) + k_{NS}\left(\Delta T_{SO,1} - \Delta T_{NO,1}\right) \quad \text{(A.2)}$$
$$f_{NL}\lambda_L \Delta T_{NL} = f_{NL}\Delta Q_{NL} + k_{LO}\left(\Delta T_{NO,1} - \Delta T_{NL}\right) \quad \text{(A.3)}$$
$$f_{SO}\lambda_O \Delta T_{SO,1} = f_{SO}\Delta Q_{SO} + k_{LO}\left(\Delta T_{SL} - \Delta T_{SO,1}\right) + k_{NS}\left(\Delta T_{NO,1} - \Delta T_{SO,1}\right) \quad \text{(A.4)}$$
$$f_{SL}\lambda_L \Delta T_{SL} = f_{SL}\Delta Q_{SL} + k_{LO}\left(\Delta T_{SO,1} - \Delta T_{SL}\right) \quad \text{(A.5)}$$

with f_{XX} as the area fraction, k_{LO} as the land-ocean exchange coefficient and k_{NS} as the northern-southern hemisphere exchange coefficient.

By formulating one equation for each hemisphere, the following equations are brought back from Equations A.2 and A.3, and, A.4 and A.5:

$$f_{NO}\lambda_O \Delta T_{NO,1} = f_{NO}\Delta Q_{NO} + f_{NL}\Delta Q_{NL} - f_{NL}\lambda_L \Delta T_{NL} + k_{NS}\left(\Delta T_{SO,1} - \Delta T_{NO,1}\right) \quad \text{(A.6)}$$
$$f_{SO}\lambda_O \Delta T_{SO,1} = f_{SO}\Delta Q_{SO} + f_{SL}\Delta Q_{SL} - f_{SL}\lambda_L \Delta T_{SL} + k_{NS}\left(\Delta T_{NO,1} - \Delta T_{SO,1}\right) \quad \text{(A.7)}$$

The sum of A.6 and A.7 returns the following equation, given the fact that the total fraction of the ocean (f_O) is a sum of the oceanic fractions of the two hemispheres ($f_{NO} + f_{SO}$), the total fraction of land (f_L)is a sum of the land fractions of the two hemispheres ($f_{NL} + f_{SL}$) and the total change in radiative forcing (ΔQ) is a sum of the four radiative forcings per box:

(ΔQ_{NO}+ΔQ_{NL}+ΔQ_{SO}+ΔQ_{SL}):

$$f_O\lambda_O \Delta T_{O,1} + f_L\lambda_L \Delta T_L = \Delta Q \quad \text{(A.8)}$$

The combination of Equations A.1 and A.8 and inclusion of the ratio R ($= \Delta T_L / \Delta T_{O,1}$) brings back the following relationship:

$$f_O\lambda_O + f_L\lambda_L R = \lambda\left(f_O + f_L R\right) \quad \text{(A.9)}$$

In other words:

$$\lambda_L = \left\{\lambda\left(f_O + f_L R\right) - f_O \lambda_O\right\} \Big/ f_L R \qquad \text{(A.10)}$$

With a stated value of *R*, the only unknown parameters in A.10 are λ_O and λ_L. To determine both values, an iterative calculation is performed: first, a trial value for λ_O is chosen, and then λ_L calculated with Equation A.10; next, the temperature changes in Equations A.2-5 are calculated until the output value of the land/ocean temperature ratio is the same as the input *R*. For this calculation, the Equations A.2-5 can be written in a matrix form:

$$\underline{\underline{C}} \cdot \underline{\Delta T} = \underline{Q} \qquad \text{(A.11)}$$

with:

$$\underline{\underline{C}} = \begin{bmatrix} f_{NO}\lambda_O + k_{LO} + k_{NS} & -k_{LO} & -k_{NS} & 0 \\ -k_{LO} & f_{NL}\lambda_L + k_{LO} & 0 & 0 \\ -k_{NS} & 0 & f_{SO}\lambda_O + k_{LO} + k_{NS} & -k_{LO} \\ 0 & 0 & -k_{LO} & f_{SL}\lambda_L + k_{LO} \end{bmatrix}$$

$$\left[\Delta T\right]^T = \begin{bmatrix} \Delta T_{NO,1} & \Delta T_{NL} & \Delta T_{SO,1} & \Delta T_{SL} \end{bmatrix}$$

$$\left[Q\right]^T = \begin{bmatrix} f_{NO}\Delta Q & f_{NL}\Delta Q & f_{SO}\Delta Q & f_{SL}\Delta Q \end{bmatrix}$$

To calculate the temperature changes, the following calculation returns a unique solution:

$$\underline{\Delta T} = \underline{\underline{C}}^{-1} \cdot \underline{Q}$$

Hence, this iterative calculation returns two different sensitivity coefficients above land (λ_L) and ocean (λ_O) determined by the predefined ratio *R*.

This subroutine within UDCM of IMAGE 2.2 is called during the initialisation of IMAGE 2.2.

Appendix B: Mathematical details of UDCM

As explained in section 5.1, the temperature increase of each oceanic layer needs to be calculated to determine the global-mean surface temperature change. From section 5.1 we obtained the following three equations from section 5.1:

$$f_{NO}\left(\rho\cdot c\cdot h_m\frac{d\Delta T_{NO,1}}{dt}-\Delta Q_{NO}+\lambda_O\Delta T_{NO,1}+\Delta F_{NO}\right)= f_{NL}\Delta Q_{NL}-f_{NL}\lambda_{NL}\Delta T_{NL}+k_{NS}\left(\Delta T_{SO,1}-\Delta T_{NO,1}\right) \tag{5.8}$$

$$\Delta F_{NO}=\frac{\rho\cdot c\cdot K\left(\Delta T_{NO,1}-\Delta T_{NO,2}\right)}{0.5d}-\rho\cdot c\cdot w\left(\Delta T_{NO,2}-\pi\cdot\Delta T_{NO,1}\right) \tag{5.12}$$

$$\Delta T_{NL}=\frac{f_{NL}\Delta Q_{NL}}{f_{NL}\cdot\lambda_L+k_{LO}}+\frac{k_{LO}\Delta T_{NO,1}}{f_{NL}\cdot\lambda_L+k_{LO}} \tag{5.13}$$

In the following calculation we want to know the change in temperature in the oceanic mixed layer. Hence, we implement Equations 5.12 and 5.13 in Equation 5.8. After the implementation of Equation 5.12, we get the following equation:

$$\frac{d\Delta T_{NO,1}}{dt}=\frac{\Delta Q_{NO}}{\rho\cdot c\cdot h_m}-\frac{\lambda_O\Delta T_{NO,1}}{\rho\cdot c\cdot h_m}-\frac{K\left(\Delta T_{NO,1}-\Delta T_{NO,2}\right)}{0.5\cdot d\cdot h_m}+\frac{w\left(\Delta T_{NO,2}-\pi\cdot\Delta T_{NO,1}\right)}{h_m} +\frac{f_{NL}\cdot\Delta Q_{NL}}{f_{NO}\cdot\rho\cdot c\cdot h_m}-\frac{f_{NL}\cdot\lambda_L\cdot\Delta T_{NL}}{f_{NO}\cdot\rho\cdot c\cdot h_m}+\frac{k_{ns}\left(\Delta T_{SO,1}-\Delta T_{NO,1}\right)}{f_{NL}\cdot\rho\cdot c\cdot h_m} \tag{B.1}$$

Next, ΔT_{NL} from Equation 5.13 can be substituted in Equation B.1. At the same time we write the equation in discrete timesteps. This returns the following equation for the temperature change of the mixed layer (with in superscript the different timesteps t and t+1):

$$\Delta T_{NO,1}^{t+1}-\Delta T_{NO,1}^{t}= \underbrace{\frac{\Delta t}{\rho\cdot c\cdot h_m}\Delta Q_{NO}^{t}}_{\text{forcing term}}-\underbrace{\frac{\lambda_O\Delta t}{\rho\cdot c\cdot h_m}\Delta T_{NO,1}^{t+1}}_{\text{feedback term}}-\underbrace{\frac{K\Delta t}{0.5\cdot d\cdot h_m}\left(\Delta T_{NO,1}^{t+1}-\Delta T_{NO,2}^{t+1}\right)}_{\text{diffusion term}}+$$

$$\underbrace{\frac{w^t\Delta t}{h_m}\left(\Delta T_{NO,2}^{t+1}-\pi\Delta T_{NO,1}^{t+1}\right)}_{\text{downwelling term}}+\underbrace{\frac{\Delta t}{\rho\cdot c\cdot h_m}\frac{k_{LO}}{f_{NO}}\frac{\left(\Delta Q_{NL}^{t}-\lambda_L\Delta T_{NO,1}^{t+1}\right)}{\left(\frac{k_{LO}}{f_{NL}}+\lambda_L\right)}}_{\text{land forcing term}}+ \tag{B.2}$$

$$\underbrace{\frac{\Delta t}{\rho\cdot c\cdot h_m}\frac{k_{NS}}{f_{NO}}\left(\Delta T_{SO,1}^{t}-\Delta T_{NO,1}^{t}\right)}_{\text{interhemispheric exchange term}}$$

The layers beneath the mixed layer are only dependent on upwelling and diffusion. Hence, the mean temperature change of the second layer (N=2 in Figure 5.3) is calculated as follows:

$$\Delta T_{NO,2}^{t+1} - \Delta T_{NO,2}^{t} = \frac{K\Delta t}{0.5 \cdot d^2}\left(\Delta T_{NO,1}^{t+1} - \Delta T_{NO,2}^{t+1}\right) - \frac{K\Delta t}{d^2}\left(\Delta T_{NO,2}^{t+1} - \Delta T_{NO,3}^{t+1}\right) + \frac{w^t \Delta t}{d}\left(\Delta T_{NO,3}^{t+1} - \Delta T_{NO,2}^{t+1}\right) \quad \text{(B.3)}$$

This method can be repeated from the 3rd to the 39th layer:

$$\Delta T_{NO,i}^{t+1} - \Delta T_{NO,i}^{t} = \frac{K\Delta t}{d^2}\left(\Delta T_{NO,(i-1)}^{t+1} - \Delta T_{NO,i}^{t+1}\right) - \frac{K\Delta t}{d^2}\left(\Delta T_{NO,i}^{t+1} - \Delta T_{NO,(i+1)}^{t+1}\right) + \frac{w^t \Delta t}{d}\left(\Delta T_{NO,(i+1)}^{t+1} - \Delta T_{NO,i}^{t+1}\right) \quad \text{(B.4)}$$

where the index *i* varies from 3 to 39.

Finally, the mean temperature change in the bottom layer (N=40 in Figure 5.3) has to be described with an extra term for the downwelling process (see Equation 5.9):

$$\Delta T_{NO,40}^{t+1} - \Delta T_{NO,40}^{t} = \frac{K\Delta t}{d^2}\left(\Delta T_{NO,39}^{t+1} - \Delta T_{NO,40}^{t+1}\right) + \frac{w^t \Delta t}{d}\left(\pi \Delta T_{NO,1}^{t} - \Delta T_{NO,40}^{t+1}\right) \quad \text{(B.5)}$$

To implement Equations B.2, B.3, B.4 and B.5 in the FORTRAN code, the equations have to be rewritten. The following method puts all the terms for $\Delta T_{NO,i}^{t+1}$ in index A, for $\Delta T_{NO,i+1}^{t+1}$ in index B, for $\Delta T_{NO,i-1}^{t+1}$ in index C and the rest in index D (i = 1,…,40). This returns the following algorithm:

$$A(i) \cdot \Delta T_{NO,i}^{t+1} + B(i) \cdot \Delta T_{NO,(i+1)}^{t+1} + C(i) \cdot \Delta T_{NO,(i-1)}^{t+1} = D(i) \quad \text{(B.6)}$$

where *i* indicates the ocean layers from 1 to 40.

Logically, Equation B.6 rewritten returns no value for C(1). Hence, the indices A, B and D for the mixed layer are:

$$A(1) = 1.0 + \underbrace{\frac{K\Delta t}{0.5 \cdot d \cdot h_m}}_{\text{diffusion term}} + \underbrace{\frac{w^t \Delta t}{h_m}\pi}_{\text{downwelling term}} + \frac{\Delta t}{h_m}\left(\underbrace{\frac{\lambda_O}{\rho \cdot c}}_{\text{feedback term}} + \underbrace{\frac{\lambda_L \cdot k_{LO} \cdot f_{NL}}{\rho \cdot c \cdot f_{NO}\left(k_{LO} + f_{NL} \cdot \lambda_L\right)}}_{\text{land forcing term}} \right)$$

$$B(1) = -\underbrace{\frac{K\Delta t}{0.5 \cdot d \cdot h_m}}_{\text{diffusion term}} - \underbrace{\frac{w^t \Delta t}{h_m}}_{\text{downwelling term}} \qquad \text{(B.7)}$$

$$D(1) = \Delta T^t_{NO,1} + \frac{\Delta t}{\rho \cdot c \cdot h_m}\left(\underbrace{\Delta Q_{NO}}_{\text{forcing term}} + \underbrace{\frac{\Delta Q_{NL} \cdot k_{LO} \cdot f_{NL}}{f_{NO}\left(k_{LO} + f_{NL} \cdot \lambda_L\right)}}_{\text{land forcing term}} + \underbrace{\frac{k_{NS}}{f_{NO}}\left(\Delta T^t_{SO,1} - \Delta T^t_{NO,1}\right)}_{\text{interhemispheric exchange term}} \right)$$

and in the same way for the Equations B.3 and B.4:

$$A(i) = 1.0 + \frac{K\Delta t}{d^2} + \frac{K\Delta t}{X \cdot d^2} + \frac{w^t \Delta t}{d}$$

$$B(i) = -\frac{K\Delta t}{d^2} - \frac{w^t \Delta t}{d} \qquad \text{(B.8)}$$

$$C(i) = -\frac{K\Delta t}{X \cdot d^2}$$

$$D(i) = \Delta T^t_{NO,i}$$

where $i = 2,\ldots,39$ and $X = 0.5$ for $i = 2$ and $X = 1.0$ for $i = 3,\ldots 39$.
And for the bottom layer (no value for *B(40)*):

$$A(40) = 1.0 + \frac{K\Delta t}{d^2} + \frac{w^t \Delta t}{d}$$

$$C(40) = -\frac{K\Delta t}{d^2} \qquad \text{(B.9)}$$

$$D(40) = \Delta T^t_{NO,40} + \frac{w^t \Delta t}{d}\pi \Delta T^t_{NO,1}$$

For each layer, the mean temperature change has to be calculated. Elaboration of Equations B.7, B.8 and B.9 in Equation B.6 returns the time loop, as given in the FORTRAN subroutine of the climate model of IMAGE 2.2. For example: $\Delta T^{t+1}_{NO,1}$ is calculated as follows:

$$\Delta T^{t+1}_{NO,1} = \frac{-B(1)}{A(1)} * \Delta T^{t+1}_{NO,2} + \frac{D(1)}{A(1)} \qquad \text{(B.10)}$$

Hence, after ten timesteps in each year, the temperature change in each oceanic layer is calculated as a result of changed radiative forcing.